Journal of Structural Geology 171 (2023) 104860

Contents lists available at ScienceDirect

Journal of Structural Geology

journal homepage: www.elsevier.com/locate/jsg

A closer look into slickensides: Deformation on and under fault surfaces

Daniel Ortega-Arroyo *, Matěj Peč

Department of Earth, Atmospheric, and Planetary Sciences, Massachusetts Institute of Technology, Cambridge, MA, 02139, USA

ARTICLE INFO

Keywords:
Fault mirror
Slickenside
Fault surface roughness
Principal slip zone
Nanograins

ABSTRACT

Accurate descriptions of natural fault surfaces and associated fault rocks are important for understanding fault zone processes and properties. Slickensides–grooved polished surfaces that record displacement and wear along faults– develop measurable roughness and characteristic microstructures during fault slip. We quantify the roughness of natural slickensides from three different fault surfaces by calculating the surfaces power spectra and height distributions and analyze the microstructures formed below the slickensides. Slickenside surfaces exhibit anisotropic self-affine roughness with corresponding mean Hurst exponents in directions parallel– 0.53 ± 0.07– and perpendicular –0.6 ± 0.1– to slip, consistent with reports from other fault surfaces. Additionally, surfaces exhibit non-Gaussian height distributions, with their skewness and kurtosis roughness parameters having noticeable dependence on the scale of observation. Below the surface, microstructural analyses reveal that S–C–C′ fabrics develop adjacent to a C-plane-parallel principal slip zone characterized by a sharp decrease in clast size and a thin (≤100 μm) nanoparticulate-rich principal slip surface (PSS). These microstructures are present in most analyzed samples suggesting they commonly form during slickenside development regardless of lithology or tectonic setting. Our results suggests that 1) PSS likely arise by progressive localization along weaker oriented fabrics 2) deformation along PSS's is energetic enough to comminute the rocks into nanometric grains, and 3) fault geometry can be further characterized by studying the height distributions of fault surfaces, which are likely to impact stress distributions and frictional responses along faults.

1. Introduction

Geologic observations indicate that slickensides – smooth, striated rock surfaces – and associated fault rocks record motion and mechanical wear between faulted blocks (e.g. Doblas, 1998; Fleuty, 1975; Lyell, 1871; Petit, 1987). The direct imprint of wear recorded along slickensides makes them particularly useful kinematic indicators (e.g. Kearse et al., 2019; Macklin et al., 2021; Otsubo et al., 2013) as well as indicators of the grain scale processes occurring during slip (e.g., Ohl et al., 2020; Siman-Tov et al., 2013., Smith et al., 2011; Toy et al., 2017; Verberne et al., 2014, 2019). Studies on natural and experimental fault surfaces are hence useful for deciphering the microphysical origins of friction and identifying active deformation mechanisms (e.g., Brodsky et al., 2020; J. Chen et al., 2020; Di Toro et al., 2011; Hadizadeh et al., 2015; Renard et al., 2012; Rice, 2006; Thom et al., 2017; Tisato et al., 2012; Verberne et al., 2014, 2019).

Slickensides further allow us to study and characterize in detail and over many scales the geometry of single fault segments (Bistacchi et al., 2011; Brodsky et al., 2016; Candela et al., 2009, 2012; Kirkpatrick et al., 2020; J.-J. Lee and Bruhn, 1996; Power et al., 1987). This is particularly important as fault geometry has been shown to be a major factor contributing to earthquake rupture nucleation, propagation and arrest (e.g., Ben-Zion and Rice, 1997; Cattania and Segall, 2021; Sagy and Lyakhovsky, 2019; Scholz, 2019; Tal et al., 2020). The irregularities on the surface geometry, known as roughness, exert a direct control on surface properties that control surface interactions such as real area of contact, friction, wear, and lubrication (e.g., Bhushan, 2013; Boneh and Reches, 2018; Bowden et al., 1939; Dieterich and Kilgore, 1996; Tal et al., 2020).

Over the last decades, studies have shown that fault roughness exhibits a self-affine geometry that spans many scales of observation (Bistacchi et al., 2011; Brodsky et al., 2016; S. R. Brown and Scholz, 1985; Candela et al., 2009, 2012; X. Chen et al., 2013; Kirkpatrick and Brodsky, 2014; J.-J. Lee and Bruhn, 1996; Power et al., 1987; Shervais and Kirkpatrick, 2016; Siman-Tov et al., 2015; Toy et al., 2017). In contrast to a self-similar geometry that is scale independent, a self-affine fractal is scale dependent. This means that to observe self-similarity, i.e., scale-invariance, an affine transformation that scales the axes of the

* Corresponding author.
E-mail address: dortega@mit.edu (D. Ortega-Arroyo).

https://doi.org/10.1016/j.jsg.2023.104860
Received 22 September 2022; Received in revised form 1 March 2023; Accepted 8 April 2023
Available online 14 April 2023

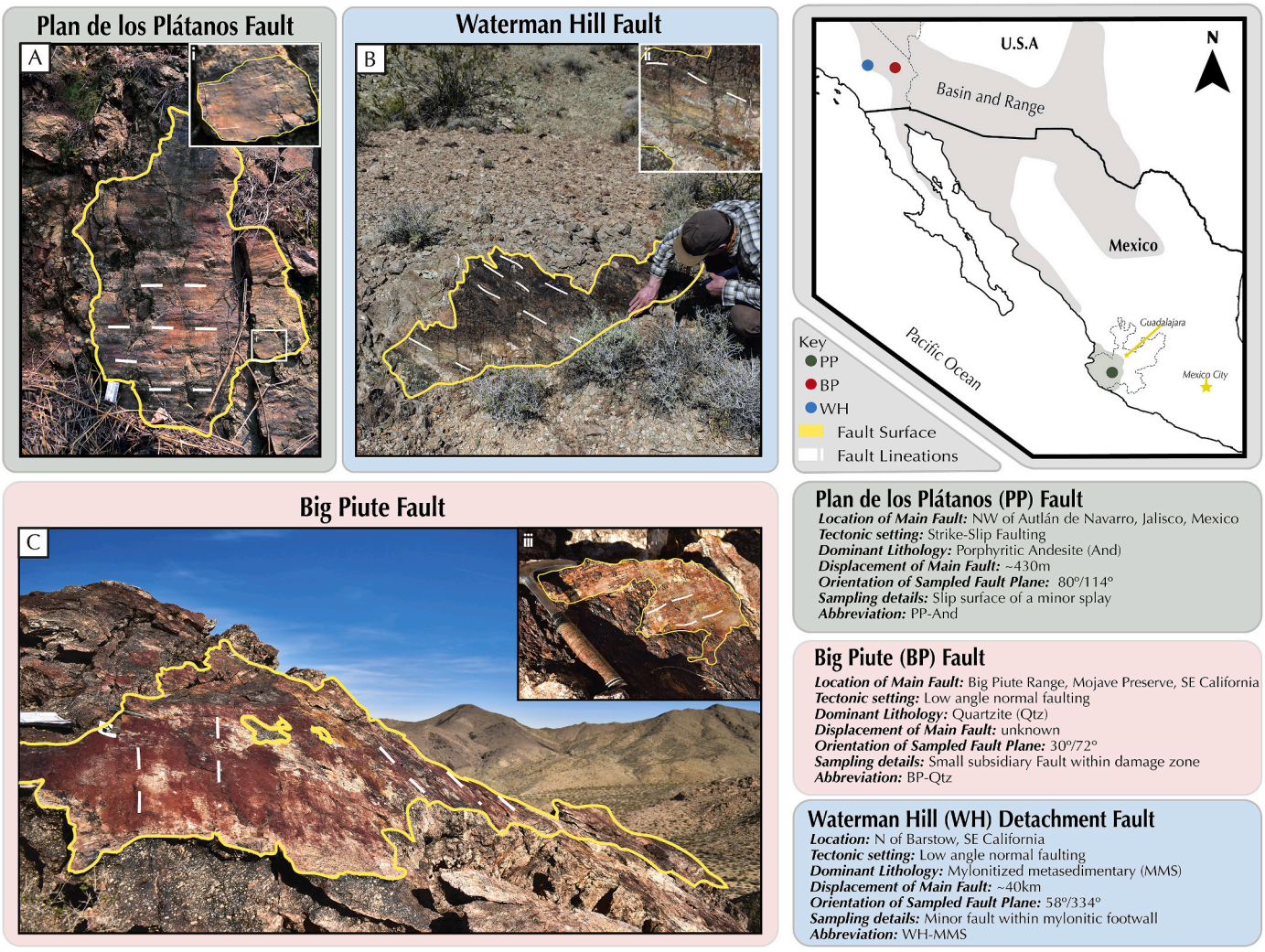

Fig. 1. Studied fault surfaces. Yellow line highlights slip surfaces and white dotted lines indicate slip lineations. A) Slickensides at the right lateral strike-slip, PP-And, ID card for scale (8.56 cm long). B) Minor slip surface cutting through the mylonitic footwall of the WH-MMS. C) Subsidiary fault within the BP-Qtz fault damage zone. Insets are close-ups of sampled regions. i-iii) Close up of fault surface used in further studies. Note: PP-, WH-, and BP- indicate the fault system, whereas And (andesite), MMS (mylonitic meta-sedimentary), and Qtz (quartzite) indicate the respective lithologies. (For interpretation of the references to color in this figure legend, the reader is referred to the Web version of this article.)

fractal surface (e.g., length vs. width) differently is needed (Mandelbrot, 1985).

Current fault zone models feature a zone of distributed fracturing with increasing intensity that culminates in a highly strained fault core characterized by an abundance of highly fractured and comminuted fault rocks (Caine et al., 1996; F. M. Chester and Logan, 1986; Faulkner et al., 2010). The architecture of fault zones is then generally described by: a) distribution and number of cores, b) width and intensity of fracturing within the damage zone, and c) distribution of subsidiary faults (Faulkner et al., 2010, 2011). Fault zones that are currently exposed experienced a number of discrete slip events that ultimately lead to fault zone development (e.g., Gold et al., 2020; Shervais and Kirkpatrick, 2016). Slickensides can form between two shearing blocks and subsequently form prominent fault surfaces.

The architecture of a fault zone, structures found within fault zones, and the strain partitioning between them, need to be known so that their potential effect on ground motion can be evaluated. Rupture models typically rely on the interaction of one or few rough fault segments (e.g., Bruhat et al., 2020; Cattania and Segall, 2021; Graves and Pitarka, 2016; Ulrich et al., 2019) with recently developed models accounting for a much larger number of interacting slip surfaces (Chu et al., 2021; Tsai et al., 2021; Tsai and Hirth, 2020).

Thus, this work aims to thoroughly describe the geometry of discrete slip surfaces and identify the dominant deformation mechanisms occurring during slip and slickenside development. We examine the surface and associated microstructures of individual principal slip structures recorded along natural slickensides from three different fault systems hosted within different lithologies. We start by studying the roughness of each slickenside using Fourier Power Spectrum Density analyses (PSD) to derive their respective Hurst exponent, otherwise known as the roughness coefficient. The geometry of the different slip surfaces is further characterized by statistically describing the height distributions of the surfaces at multiple scales of observation. Our work on slickensides is then extended beyond the surface to the fault rocks that host them by conducting detailed microstructural and grain size distribution analyses of the rock volume surrounding the fault surface. Lastly, we discuss the implications of our observation on our understanding of faulting processes.

2. Methods

We focused on slickenside surfaces collected from 3 different fault systems–a strike slip Plan de los Plátanos fault (PP) in SE Jalisco, Mexico, the Big Piute Ranges low angle normal fault (BP), and Waterman Hills

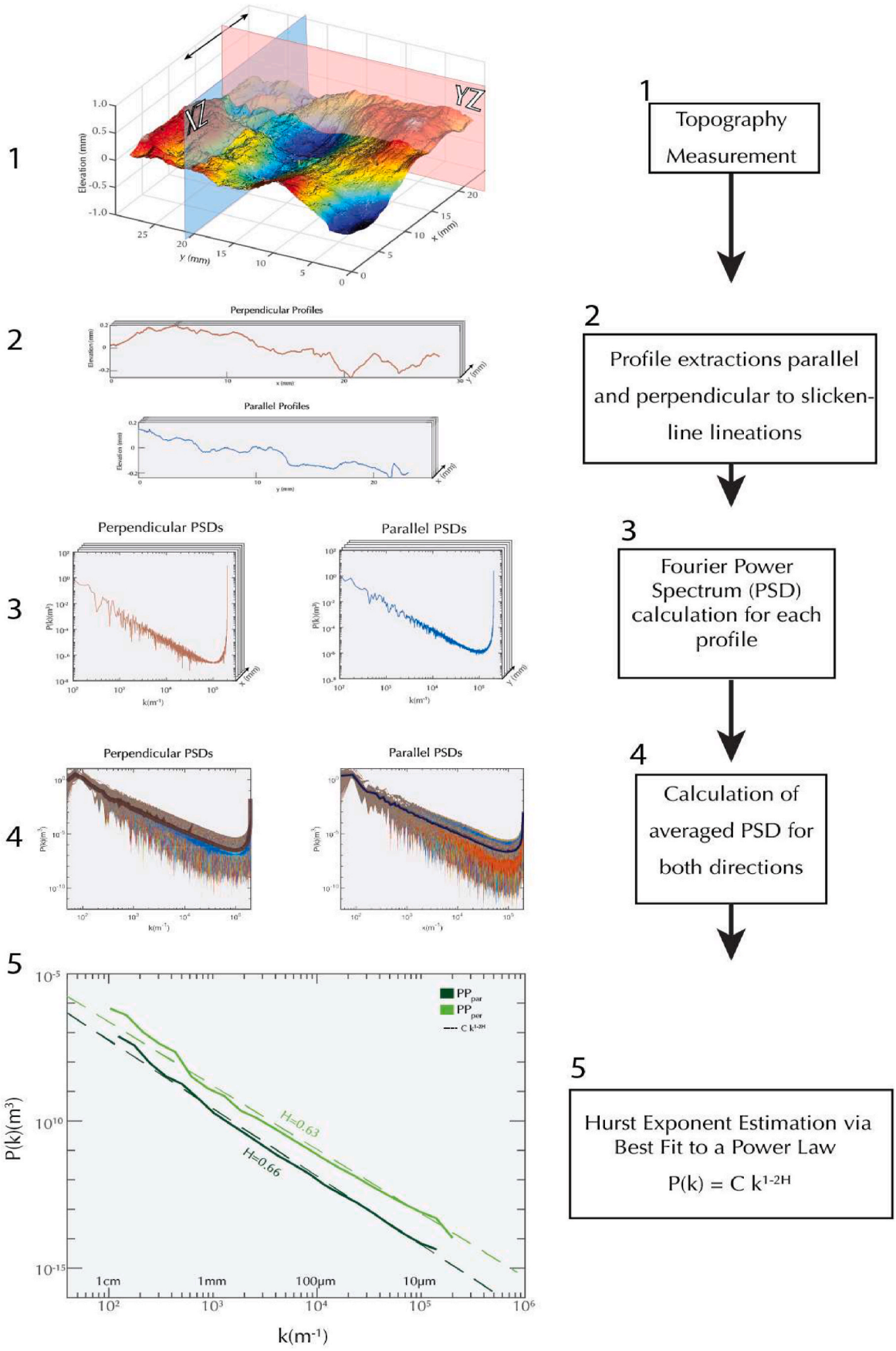

Fig. 2. Calculation of Hurst Exponent. See text for details.

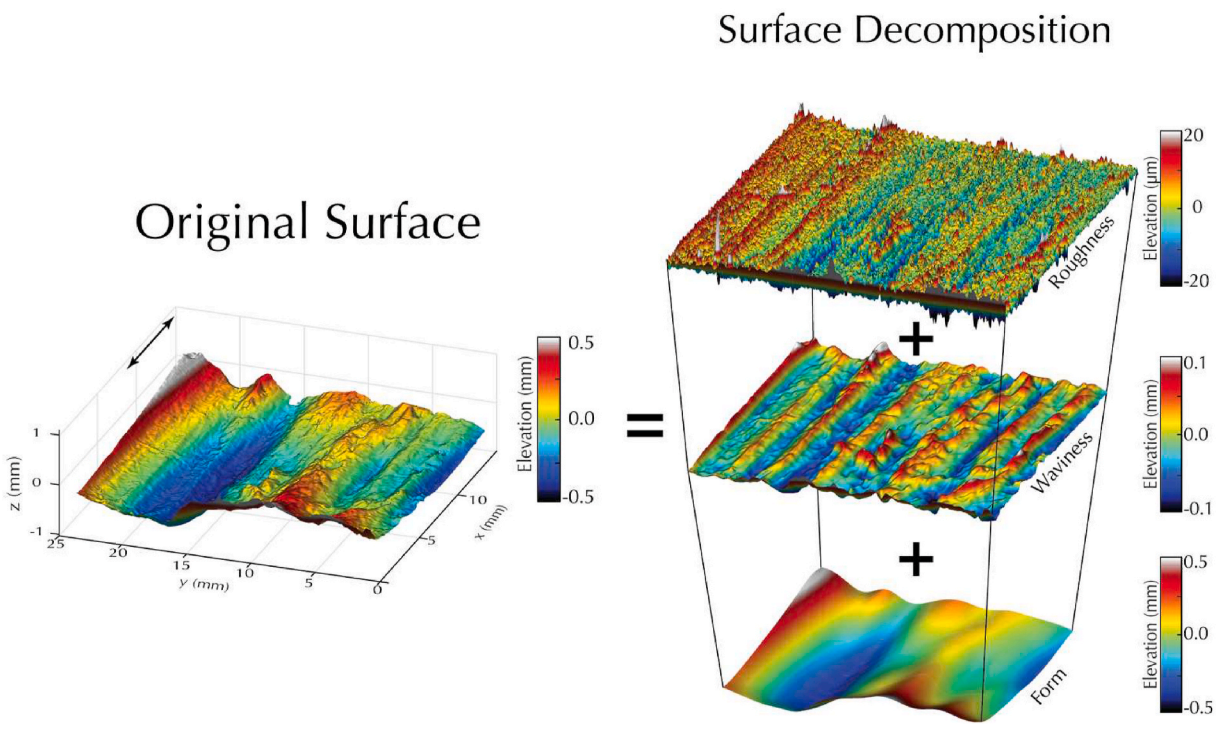

Fig. 3. Schematic of a Multiscale Surface Texture Analysis shows how a surface measurement is decomposed into characteristic wavelengths.

detachment fault (WH), both in SE California– that represent different lithologies and/or tectonic settings as summarized in Fig. 1. At each locality, we aimed to sample specimens that preserved both sides of the fault surface as further explained in the Appendix, if possible, to better capture the structures and materials that comprise slickensides. The faults–PP, BP, and WH– cut through primarily andesite (And), quartzite (Qtz), and mylonitic metasedimentary (*MMS*) rocks, respectively.

2.1. Brief geologic background of analyzed samples

2.1.1. Plan de los Plátanos fault (PP-and)

The Plan de los Plátanos is right lateral strike slip fault that accommodates ~430 m of displacement. It is located NW of Autlán de Navarro, Jalisco, Mexico within the Jalisco Block, a rigid tectonic block developed during the Miocene that moves independently from the Rivera and North American plates bounded by the Tepic-Zacoalco Rift and the Colima Rift (De la Teja Segura and Roque Ayala, 2007; Ferrari et al., 2000; Rosas-Elguera et al., 1996). The PP-And fault is a subvertical structure that cuts through Laramide-folded Tertiary andesite-rhyolite tuffs that overlay the Tepaltepec Cretaceous volcano-sedimentary sequence, intruded by the late Cretaceous-early Paleogene Tomatlan granitic batholith (De la Teja Segura and Roque Ayala, 2007).

The PP-And slickenside sample was collected from a minor splay, of unknown displacement, exposed on the side of the road near the town of Jalocote (De la Teja Segura and Roque Ayala, 2007). The sample records multiple slickenside surfaces hosted in a porphyritic andesite with sericitized plagioclase phenocrysts in the 0.1–1.0 mm range. The rock is hydrothermally altered with secondary chlorite and iron oxides comprising the bulk of the fracture fill along with few quartz-rich veins. Despite the heavy alteration and hosting of slickensides, the host rock seldom records pervasive/distributed deformation as the primary igneous texture is relatively intact a few cm away from the slip surface.

2.1.2. Big Piute normal fault (BP-Qtz)

The Big Piute Mountains lie in the eastern Mojave Desert within a late Cretaceous ductile deformation belt of synkinematic metamorphism and granitoid pluton emplacement (Hoisch et al., 1988; Miller et al., 1982; Reynolds et al., 1988). Thick-skinned thrusting places Proterozoic crystalline basement over recumbently folded Paleozoic meta-sediments (Reynolds et al., 1988; Ring et al., 1988). A sequence of Tertiary sedimentary and volcanic rocks overlies Mesozoic, Paleozoic and Proterozoic rocks. Tertiary faults cut through all strata and account for 20–30% crustal extension accommodated in the region (Fletcher and Karlstrom, 1990 and references therein).

Slickensides from this location were collected from small subsidiary faults within the damage zone of the BP-Qtz that unfortunately did not exhibit reliable displacement markers to confidently determine displacements. Unlike the other samples, the slickenside in these faults are hosted within a monomineralic quartzite host rock with a primary grain size ranging from 200 µm to 1 mm.

2.1.3. Waterman Hills fault (WH-MMS)

The Waterman Hill Detachment Fault (WH-MMS) is a low angle detachment fault thought to accommodate more than 40 km of total slip located within Central Mojave Metamorphic Core Complex exposed along the Mitchell Range N of Barstow, SE California (Glazner et al., 1989). The WH-MMS juxtaposes Tertiary sedimentary and volcanic strata against Mesozoic granodiorites and the Waterman Gneiss, which consists of mylonitized late Proterozoic to Paleozoic metasedimentary and metaigneous lithologies (Fletcher et al., 1999; Glazner et al., 1989).

The samples were collected from a minor fault exposure (with no discernible displacement markers) found within the mylonitic footwall of the WH-MMS. The fault surface occurs at the lithological boundary of metaigneous, quartzitic and metacarbonate protoliths. The slickensides are hosted within a thick cataclasite (larger than the hand samples) comprising multiple lithologies. The rock itself is overprinted by hydrothermal alteration and calcite-filled fractures.

2.2. Sample preparation

The collected hand samples were cleaned of any loose debris and dirt prior to any surface measurement. After surface measurements are performed, we prepared 20 thin sections perpendicular to the plane of the slip surface following Tikoff et al. (2019) orientation convention,

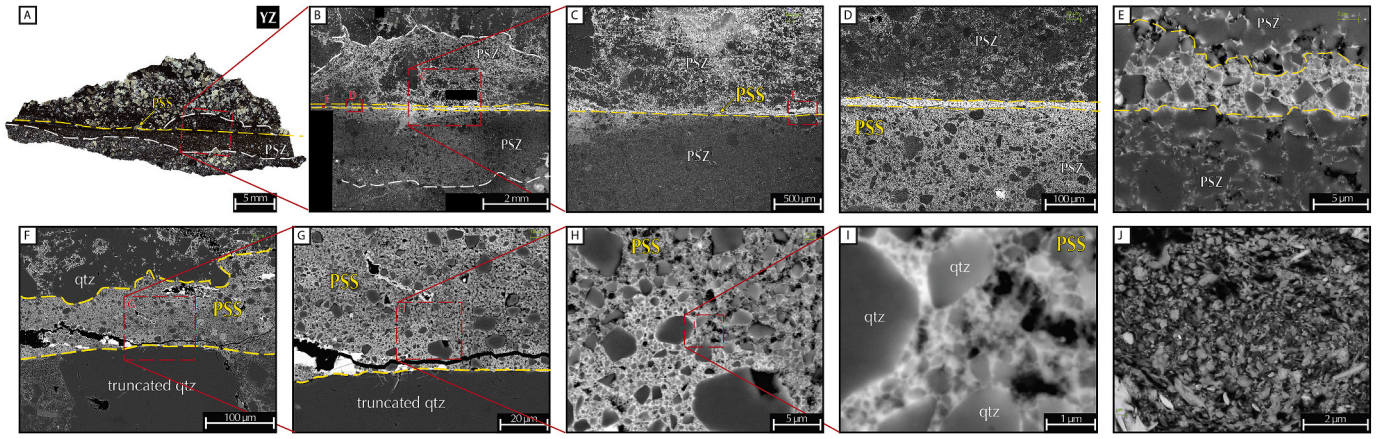

Fig. 4. Set of images at progressively higher magnifications used in the GSD determination of BP-Qtz slickenside. See text for details.

where *XZ* and *YZ* correspond to thin sections oriented parallel and perpendicular to the slip lineations, respectively, as illustrated on the surface 3-D model in Fig. 2.

2.3. Roughness analysis

We characterized and quantified the slickenside roughness of the different fault surfaces over six orders of magnitude in length scale ranging from 100's of nm to 3 cm. Each surface (between 100 mm^2 to 1000 mm^2) was measured by a Taylor Hobson TALYSCAN 150 profilometer using a no-contact laser gauge with a 252 nm vertical resolution. A constant 2 mm s^{-1} traversing speed and a 5 µm spacing were used for each measurement unless otherwise indicated.

At the micron scale, the slip surfaces' topography was measured by manually tracing the surface profile of selected thin sections imaged through Scanning Electron Microscopy (SEM).

2.3.1. Hurst Exponent calculation

The TALYSCAN 150 measurements were processed in MATLAB to remove any planar inclination trend associated with the initial sample placement on the profilometer. 1) The measurements-in the form of an elevation matrix-are then rotated such that the horizontal axis (*x*-axis) of the 3D and digital elevation models (DEM) are parallel to the slip lineations. Once the trend has been removed from the elevation matrices, we proceeded to calculate the Hurst exponent using power spectrum density analyses (PSD) (c.f., Bistacchi et al., 2011; Candela et al., 2009, 2012; Jacobs et al., 2017; Siman-Tov et al., 2013). Profiles parallel and perpendicular to the slip lineations are extracted from each surface. A one-dimensional Hann window function is then applied to each line scan to correct for measurement artifacts, particularly near the edges, as suggested by Jacobs et al. (2017). 3) The Fourier power spectrum $P(k)$ is calculated for each profile as a function of wavenumber (k) and normalized by dividing the power spectrum by the length of the corresponding profile. 4) The power spectra for both the parallel and perpendicular directions to slip are averaged at each wavenumber to reduce noise associated with each individual profile. 5) The Hurst exponent is then calculated from the best fit to a power-law of the form $P(k) = Ck^{1-2H}$, where H is the Hurst exponent, and C is the pre-factor. The workflow is illustrated in Fig. 2. The evaluation of the signal processing technique accuracy is further explained in the Appendix.

2.3.2. Multiscale surface texture analysis

Given that the roughness measurements are inherently a superposition of surface texture information from different length scales, we performed a multiscale surface texture analysis (MSA) in addition to the Hurst exponent calculation. A MSA consists of decomposing the surface topography at various cutoff wavelengths to separate the surface texture into 1) *form*, 2) *waviness* (macro-roughness), and 3) *roughness* (micro-roughness) as shown in Fig. 3 (C. A. Brown et al., 2018). We used a Gaussian 2D filter to separate the data into three different bandwidths with cutoff wavelengths centered at 5 mm and 500 µm. Care is taken that the energy of the signal is preserved, i.e., that the original signal can be fully reconstructed when all components are added together. Furthermore, for each component, we calculate the kurtosis (S_{kur}) and skewness (S_{sk}) of the height distribution.

2.4. Microstructural analyses

In order to observe the associated microstructures in the volume of rock adjacent to slickensides, we selected one sample from each locality that best preserves the slickenside features to conduct SEM-BSE imaging and describe the microstructures in greater detail. We study a) the grain size distributions and b) the morphologies and crosscutting relationships preserved in, and adjacent to the slickensides to reveal their relationship to fault surface development.

2.4.1. Imaging conditions

Thin sections oriented parallel (*XZ*) and perpendicular (*YZ*) to the slip direction were analyzed using a ZEISS AX10 Petrographic microscope and ZEISS Merlin HR-SEM equipped with a Backscattered electron (BSE) detector and an Energy Dispersive X-Ray spectrometer (SEM-EDS).

The SEM was operated with a beam current of 5 nA and a 15 kV accelerating voltage unless otherwise indicated. To capture the range of structures and grain sizes, images were acquired at various magnifications resulting in a 0.77 nm/px to 2.06 µm/px resolution.

Additionally, compositional maps of selected samples were acquired using a Bruker Tornado Micro X-Ray Fluorescence Spectrometer (XRF) operated with a beam current of 600 µA and a 50 kV accelerating voltage with a 20µm/px resolution.

2.4.2. Grain size analysis

Grain size measurements were obtained by manually tracing petrographic microscopy and BSE images obtained at progressively higher magnifications as illustrated in Fig. 4. At each magnification we trace the maximum number of discernible grains/clasts, typically 300–3000 segmented grains per image range are used. Segmented images were then imported to *ImageJ* to calculate the area (A) of each grain in pixels. Grains with areas smaller than 20 pixels, i.e., the smallest grain size that could still be clearly recognized as such, were excluded. The size of each grain is then approximated by calculating the diameter of a circle with the same area. The equivalent diameters (d_{eq}) were calculated as

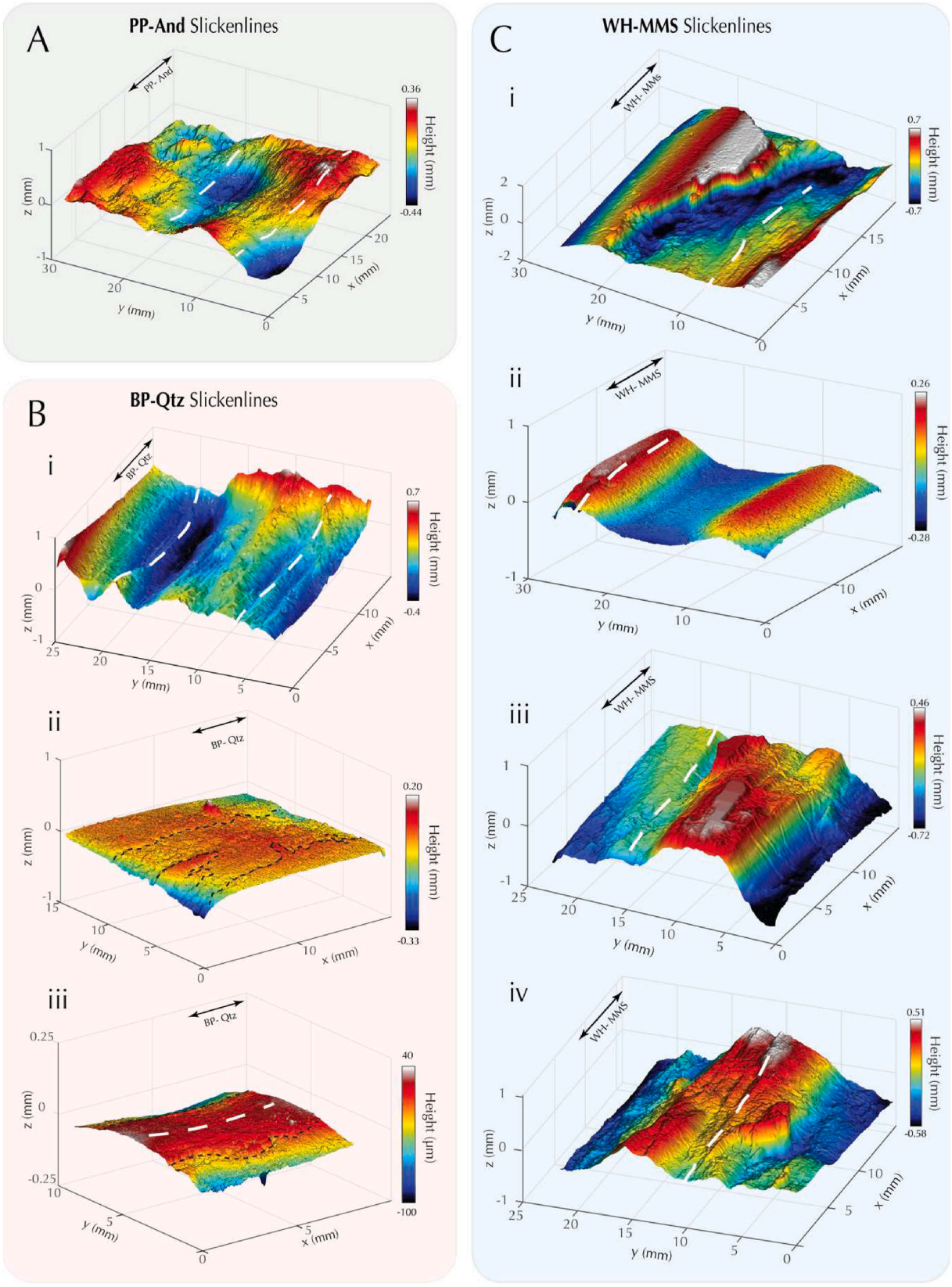

Fig. 5. Topography of the different surfaces collected via laser profilometry grouped from A) PP-And, B) BP-Qtz, and C) WH-MMS. White dotted lines highlight grooves and lineations. Black dotted lines highlight transitions in roughness.

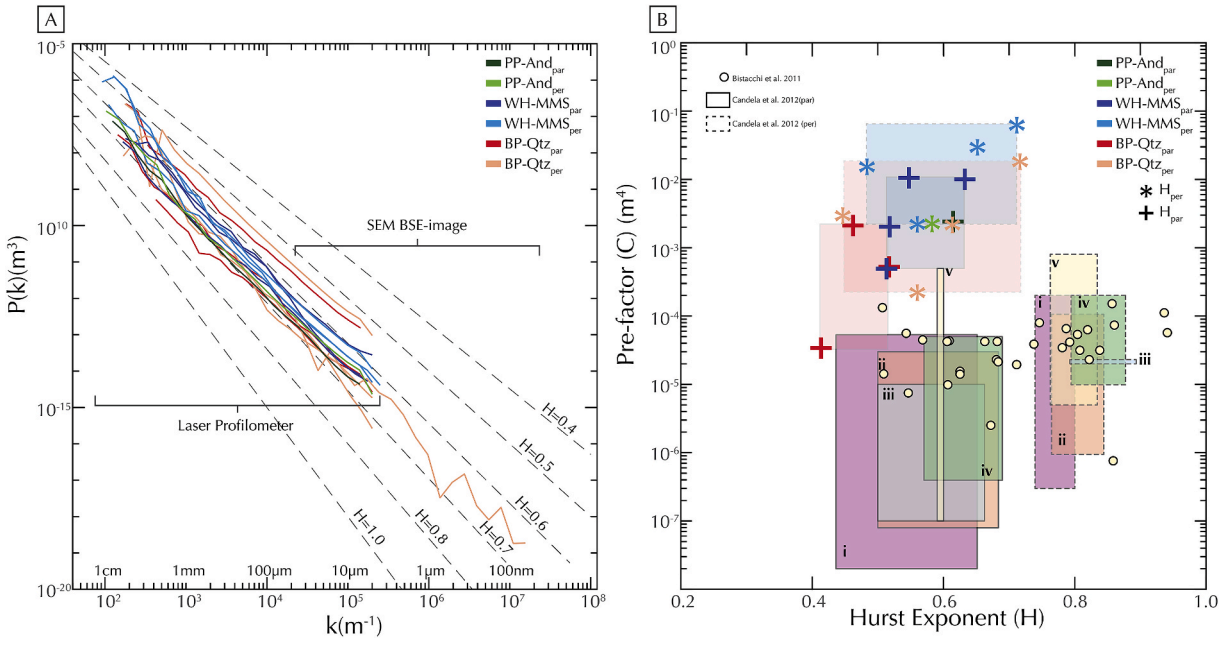

Fig. 6. Results from PSD analysis. A) Fourier power spectra for all studied samples. Note similar slopes fit most samples; rougher samples plot higher in the graph. B) Pre-factor and Hurst exponents obtained from (A), Gole Larghe Fault Zone (Bistacchi et al., 2011) and i) Bolu, ii) Vuache-Sillingy iii) Dixie Valley iv) Corona Heights and v) Magnola faults (Candela et al., 2012). Note data from (Bistacchi et al., 2011) does not specify direction of slip (circles), whereas data from (Candela et al., 2012) is plotted as a range from minimum to maximum values for H and C for both parallel (filled square) and perpendicular (squares with dash lines) directions to slip.

$$d_{eq} = 2\sqrt{\frac{A}{\pi}}, \tag{1}$$

and collected in a histogram with twenty bins for each magnification.

The bins from each magnification are plotted in a logarithmic scale to determine the slope (S_n) and intercept (I_n) of the best power-law fit. The frequency of each bin is then multiplied by a factor (L_n) that reflects the relative magnification at each image to correct for undercounting of the total number of grains from analyzing progressively smaller areas. The factor, L_n, is determined by:

$$L_n = 10^{I_{max} - I_n}, \tag{2}$$

where I_{max} corresponds to the intercept of the lowest magnification. The results from all magnifications are then combined into a single plot.

D-values of 0–2 are commonly measured in two-dimensional analyses (e.g., analysis of SEM images) and correspond D-values between 1 and 3 from three dimensional analyses such as sieving and Coulter counting (Glazner and Mills, 2012). To draw comparison with D-values reported in other studies that utilized three-dimensional methods the following conversion, $D_{2D} = D_{3D}$-1, from Heilbronner and Barrett (2014) is used.

3. Results

3.1. Roughness analysis

Roughness plays a significant role in the contact behavior of surfaces and is usually described as the deviations normal to a surface. In Fig. 5 we show the wide range of surface textures observed in the various samples studied grouped by localities/lithologies. We then analyzed the roughness of each samples using the Fourier power spectrum density approach to calculate their respective Hurst exponents followed by a multiscale analysis of the surfaces' height distributions.

3.1.1. Power spectral density results

The power spectral density (PSD) curves are obtained from profiles scanned parallel (*par*) and perpendicular (*per*) to the slip lineations, i.e., the *x*- and *y*-directions, as illustrated in Fig. 2. The averaged PSD curves for all roughness measurements are shown in Fig. 6 and the total number of profiles used for each measurement are indicated in Table A1.

Spectra for most measurements show only limited variability in the slope of profiles measured parallel to lineations with a mean Hurst exponent of 0.53 ± 0.07 and a range of 0.41–0.63. In contrast, the perpendicular profiles showed a wider variability with values of H_{per} ranging from 0.45 to 0.72 and a mean of 0.60 ± 0.10. The pre-factor is directly proportional to root mean squared roughness (*RMS*) by

$$RMS = \sqrt{\left[\frac{Ck^{-2H}}{-2H}\right]_{k_{min}}^{k_{max}}} \tag{3}$$

And thus, a higher *C* indicates overall higher roughness amplitude, whereas a lower *H* indicates a larger contribution of smaller wavelengths/higher spatial frequency, i.e., surfaces relatively rougher at smaller length scales than a self-similar surface ($H = 1$) with the same *C* would be.

While the samples studied in this paper show a relationship between the pre-factors and *H*, the inclusion of measurements from Bistacchi et al. (2011) and Candela et al. (2012) indicates no clear trend (Fig. 6B). Furthermore, measurements of the various hand samples obtained from

Table 1
Hurst (*H*) and pre-exponent (*C*).

Fault	H_{par}	H_{per}	C_{par}	C_{per}
PP-And				
	0.61	0.58	2.5×10^{-3}	2.2×10^{-3}
BP-Qtz				
Min	0.41	0.45	3.4×10^{-5}	2.2×10^{-3}
Max	0.52	0.72	2.2×10^{-3}	1.8×10^{-2}
WH-MM				
Min	0.51	0.48	4.9×10^{-4}	2.2×10^{-3}
Max	0.65	0.71	3.5×10^{-2}	6.2×10^{-2}

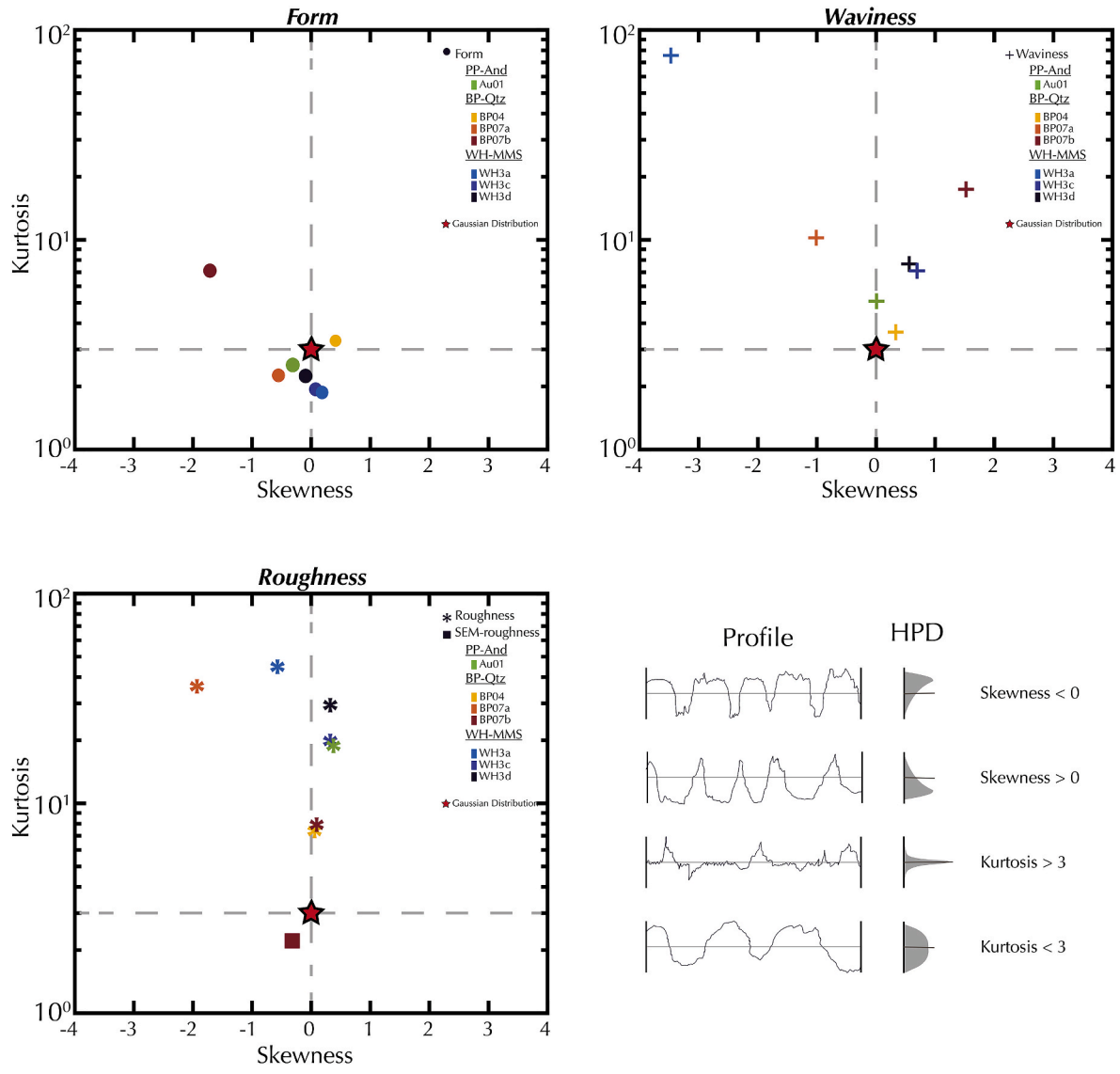

Fig. 7. Skewness and kurtosis for samples A) *Form*, B) *Waviness*, and C) *Roughness*. D) Schematic surface profiles with positive and negative skewness and kurtosis values higher and lower than three, after Gadelmawla et al. (2002).

the same fault surface show a wide range in both H and C values, Table 1.

3.1.2. Height distributions

Skewness (S_{sk}) and kurtosis (S_{kur}) are statistical measures that describe the symmetry and peakedness of the height distributions. A distribution is known as a Gaussian when $S_{sk} = 0$ and $S_{kur} = 3$. A high kurtosis ($S_{kur} > 3$) corresponds to a distribution with a greater peakedness than a Gaussian, which indicates more height measurements are centered near the mean height, whereas the converse is true for a low kurtosis ($S_{kur} < 3$). Furthermore, a positive and negative skewness indicates most measurements lie either below or above the mean surface, respectively, as illustrated in Fig. 7A. The samples show a wide range of S_{sk} and S_{kur} values, with no systematic variation with respect to lithology or fault system. However, samples wherein lineations are more apparent and visually rougher tend to have more positive skewness whereas, kurtosis is generally higher for smoother samples. The departure from a Gaussian height distribution also appears to be affected by the scale of observation with smaller wavelength having overall higher kurtosis values as documented in Fig. 7A–C. Note also surface decomposition in Fig. 3, which illustrates the distinct roughness at different scales.

3.2. Structural and microstructural observations

With the aim of interpreting the processes involved in fault slip and slickenside development, we selected one sample from each locality that best preserves the slickenside features to conduct SEM-BSE imaging to describe the microstructures in greater detail. We focused on the morphologies at the surface and throughout the rock volume adjacent to the slip surface. For each sample, we specifically examine a) the size and spacing of the lineations, b) orientation of structures on the slip surface, c) the structures within the host rock immediately adjacent to the slip surface, and d) the grain size distribution.

3.2.1. Plan de los Plátanos fault (PP-and)

The main slip surface is covered by a thin film that is glossy and smooth, with specularly reflective patches. The lineations have an average width of 527 ± 83 μm and spacing of 0.85 ± 0.18 mm that remain relatively constant throughout the length of the sample (Fig. 5A). Secondary fractures perpendicular and diagonal to the lineations crosscut the surface.

Below the exposed surface, we identified weakly developed S–C-like fabrics, highlighted by Fe- and Ti-rich phases, and a quartz-rich vein that

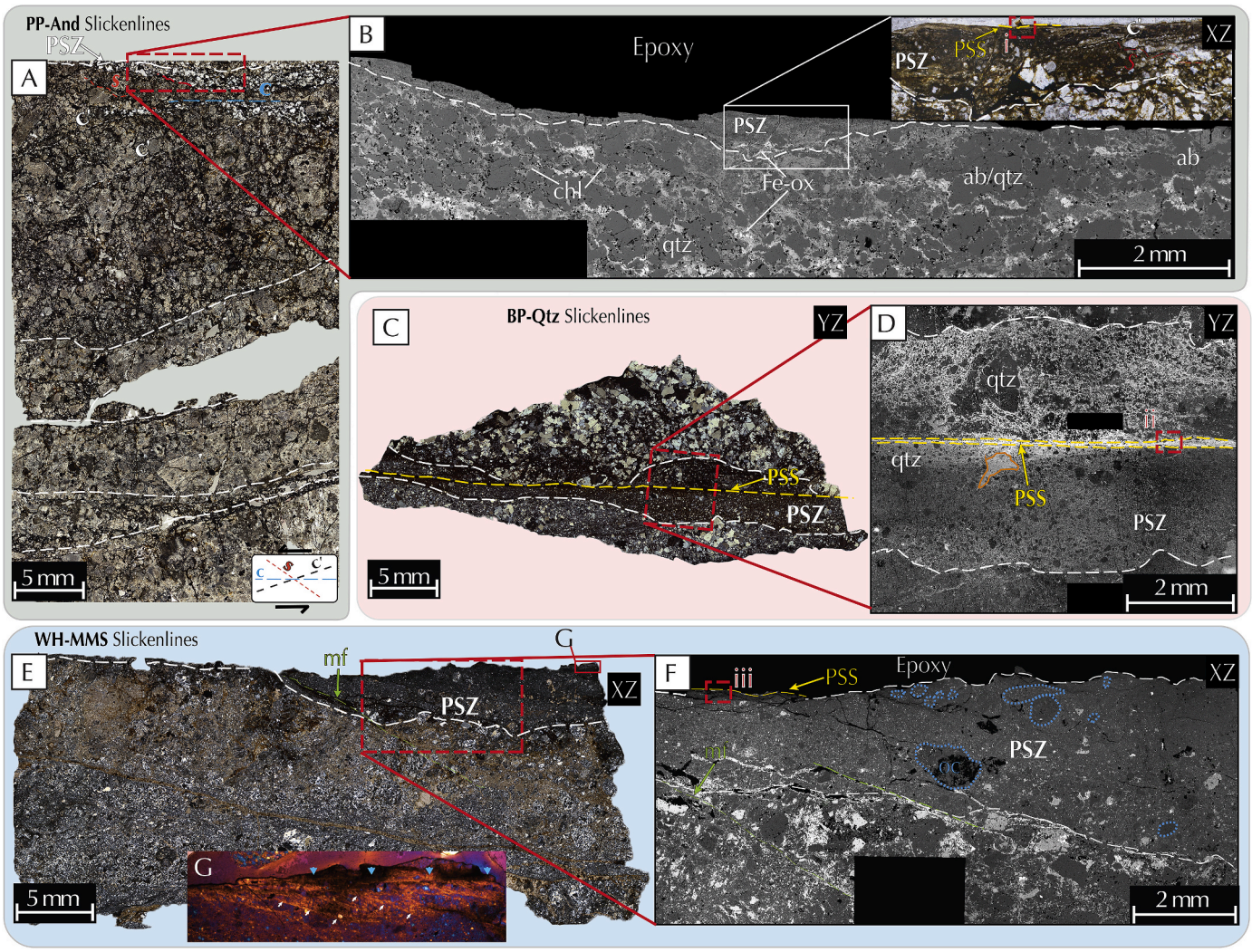

Fig. 8. Selected samples for microstructural analysis. White and yellow dashed lines highlight Principal Slip Zones (PSZ) and Principal Slip Surfaces (PSS), respectively. A) PP-And slickenside thin sections under plane-polarized light (PPL). Note relatively undeformed primary igneous fabric at the bottom of the image and multiple slip zones. B) SEM-BSE close-up of A. characterized as a zone of highly comminuted grains of irregular thickness. Dark grey colors correspond to quartz (qtz) and albite (ab), bright grey chlorite (chl), white Fe-ox, whereas black spots within the rock volume correspond to porosity. Note S–C cataclasite with top to the left sense of shear. Inset: PPL close-up of PSZ fluidized ultra cataclasite. Note tails around larger clasts. C) BP-Qtz slickensides under cross polarized light (XPL), preserving opposing segments of the fault surface. D) SEM-BSE close-up of C. Note the principal slip zone (PSZ) is characterized by highly comminuted grains in the μm-size range, whereas the principal slip surface (PSS-yellow) is localized to few tens of microns and decorated by an abundance of Fe-oxide minerals (bright colors). Note asymmetry in Fe-oxide distribution and comminution between both sides of the fault. Charging artifact denoted by orange lines. E) WH-MMS slickenside under XPL. F) Close-up of E shows the presence of a Principal Slip Zone (PSZ) of variable thickness characterized by sharp grain size reduction towards the slip surface and towards a thin Principal Slip Surface (PSS). Note the presence of older cataclastic clasts (OC) within the PSZ. Micro-faults (mf-green) are also observed offsetting the PSZ. G) Close-up of E under XPL with gypsum lambda plate inserted highlights region adjacent to surface where localized shear bands (two main orientations outlined by white and teal arrows) exhibit strong and spatially coherent optical anisotropy. Note i-iii) indicate regions analyzed further in Fig. 10. (For interpretation of the references to color in this figure legend, the reader is referred to the Web version of this article.)

soles into the slip surface (Fig. 8A–B and Fig. A5). All fabrics are then cut by a principal slip zone (PSZ) comprising a fluidized ultracataclasite of variable thickness (100–500 μm) that is characterized by a sharp decrease in grain size from the host rock towards the slip surface (Fig. 8A–B and Fig. A3). In addition to the main exposed surface, other minor slip surfaces were identified splaying within the sample (Fig. 8A).

The PSZ features a quartz-rich zone (~10 μm thick) of increased cohesion (ICZ) next to the surface, wherein grains exhibit serrated, interlocked grain boundaries, triple junctions, and sintering microstructures, followed by sharp break towards a ~5 μm thin principal slip surface (PSS) (Fig. 10A and 11A and A6).

The PSS is characterized by a predominance of mostly rounded submicron-size grains/particles embedded within "*wispy*" phyllosilicate-like matrix enriched in Al and Fe compared to the PSZ (Fig. 10A and 11A and A4). In regions where the PSS is thicker, the PSS exhibits a denser morphology with little to no porosity, albeit fractured, with similarly rounded nm-size grains/particles as well as elongated grains preferentially aligned subparallel to the surface (Fig. 10B).

3.2.2. *Big Piute slickensides (BP-Qtz)*

The slip surfaces are flat and smooth, i.e., no grooves are perceived with the naked eye, particularly in the direction parallel to the lineations, observed as alternating smeared iron oxide rich bands. When observed through the laser profilometer scans, the lineations are marked by 1–3 mm wide grooves with a spacing of 8.2 ± 0.5 mm (Fig. 5 Bii-iii).

Across the XZ orientation, the sample exhibits a foliated cataclasite microstructure with an S–C–C′ fabric that transitions into the PSZ and PSS (Fig. 9A and B). The foliations are defined by sigmoidal dark brown

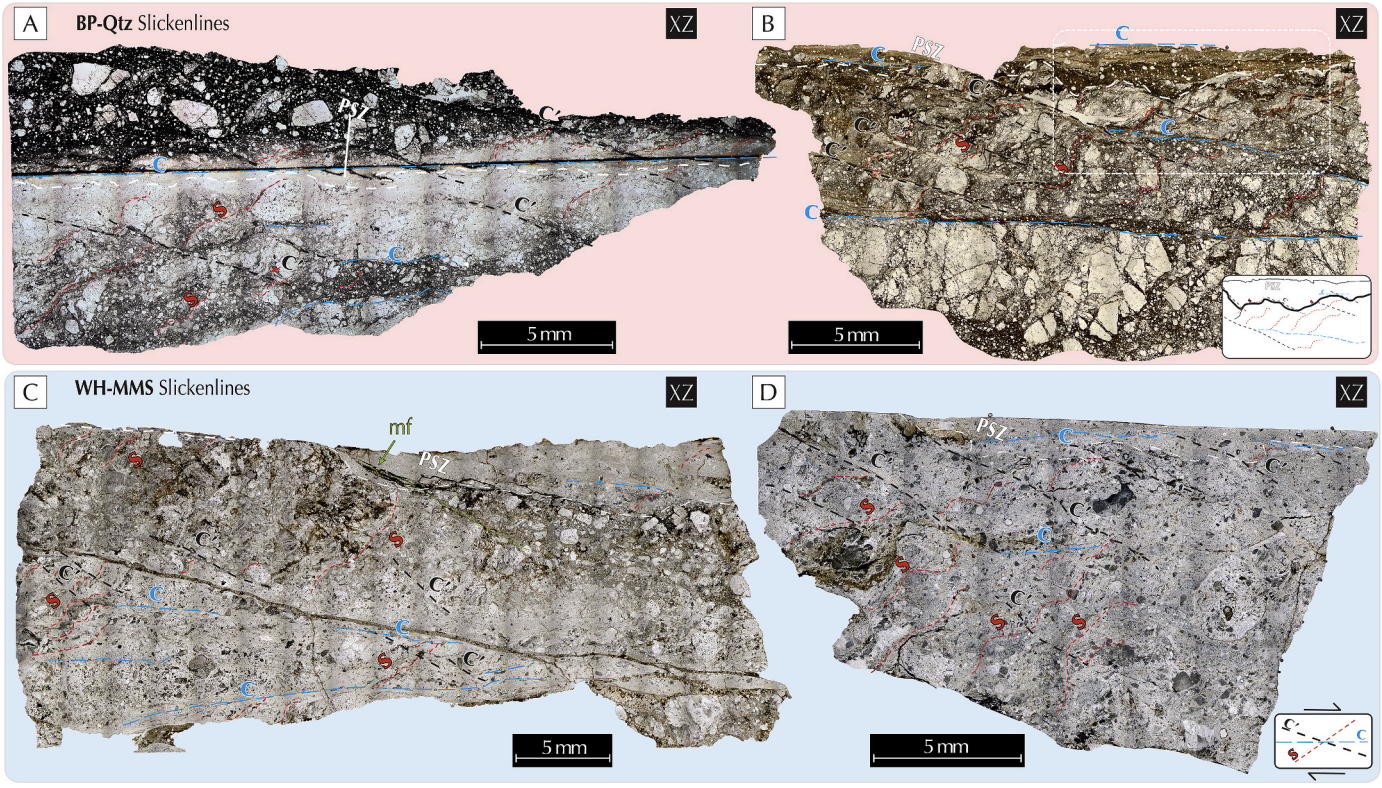

Fig. 9. PPL photomicrographs of foliated cataclasites with S–C–C′ fabrics. S-, C- and C′- planes outlined by dotted red, blue, and black lines, respectively. Vertical shaded strips are artifacts from stitching of images. PSZ outlined by thin white dashed line characterized by a sharp decrease in grain size. Note C-planes are parallel to PSS and undulation in PSZ contact follow the edges of S-, C-, and C′-planes. A-B) BP-Qtz slickensides and C-D) WH-MMS slickensides. Inset in B) is a schematic sketch of the observed S–C–C′ near the PSZ. Note border between PSZ and host exploits S-,C-,and C′-planes. (For interpretation of the references to color in this figure legend, the reader is referred to the Web version of this article.)

layers that bound asymmetric quartzite clasts and clast aggregates with their *tails* preferentially oriented ~45° to the fault surface (S-foliation), C′-shear bands developed oblique to the S- and C- orientations, and localized micro-shears sub-parallel to the slickenside surface (C-surface) (F. M. Chester et al., 1985; A. Lin, 2001; Passchier and Trouw, 2005). The boundary between the host rock and the PSZ exploits the local orientation of the S-, C-, or C′- planes as sketched in the inset of Fig. 9B.

The clast size of the cataclasite and spacing between S–C-planes gradually fines and rotate until it transitions into an ultracataclasite that makes up the PSZ and a 18 ± 11 μm thin PSS. (Fig. 8C and D, 9A-B, and 10C-D). The PSS is characterized by truncation and plucking of grains from the PSZ and matrix comprising rounded nanometric grains with little to no fractures cemented by a matrix of Fe-ox. Void spaces along fractures within the PSS are then filled by growth of Fe-ox (Figs. 4 and 10C, A8) and quartz (Fig. A8).

3.2.3. *Waterman Hill slickensides (WH-MMS)*

The surface forms a resistant ledge, is smooth and specularly reflective. The lineations are marked by cm-scale undulations within mirror-polished regions and by 520 ± 160 μm wide grooves in portions of the surface that are not specularly reflective.

We observe that the WH-MMS slickenside samples also exhibit a region of extremely comminuted grains, PSZ, adjacent to the slip surface, and S–C-like fabrics throughout its host rock (Fig. 9C and D). Unlike the other samples, the PSZ here varies significantly in thickness, from ~100 μm to 5 mm, along the direction of slip (*XZ*). Regions where the PSZ is thicker coincide with numerous micro-faults, subparallel to the C′- planes and highlighted by Fe-ox, that displace the PSZ but do not crosscut the mirror-polished surface (Fig. 8E and F and 9C). The PSZ contains clasts of earlier, more consolidated cataclasites (OC). Immediately adjacent to the slip surface, two main features are prominent: a) the presence of Riedel-like and boundary (subparallel to the slip surface) shear bands that exhibit extreme grain size reduction and uniform optical anisotropy (Fig. 8G), and b) a dense thin film (PSS) that coats the PSZ that features elongated grains preferentially oriented subparallel to the surface embedded within a dense matrix without any resolvable structure in field emission SEM (Fig. 10F), similar to Fig. 10B. Nanosized grains are also observed to be common within the matrix of the PSZ.

3.3. *Grain size distribution*

To characterize the comminution processes occurring during slip, we analyzed the grain size distribution of the fault rocks adjacent to the slip surface. Here we present the results of the grain size analyses performed on two sequences of petrographic microscopy and SEM images taken at increasing magnifications from selected samples from the BP-Qtz (Fig. 4) and PP-And faults (Fig. A3). The results are plotted on log-log plots of normalized particle frequency vs. equivalent diameter to determine the fractal grain size distribution (GSD), Fig. 12.

We did not perform grain size analysis on samples from WH-MMS. It was not possible to accurately identify individual grain boundaries as the particles appear embedded within a cement of similar composition. Furthermore, when the boundaries between particles could be accurately identified, they exhibit interlocked grain boundaries and triple junctions, suggesting static crystal growth and healing (Keulen et al., 2008), and thus obscuring the grain sizes related to the comminution process, Fig. A10.

The grain size distribution for the quartzite sample shows a power-law functional relationship over six orders of magnitude (10's nm-1's mm) with a constant slope *of D = 2.67 ± 0.03* despite the sharp decreases in grain size observed within the transition from the host rock towards the PSZ and PSS respectively, Fig. 8C and D. However, it is

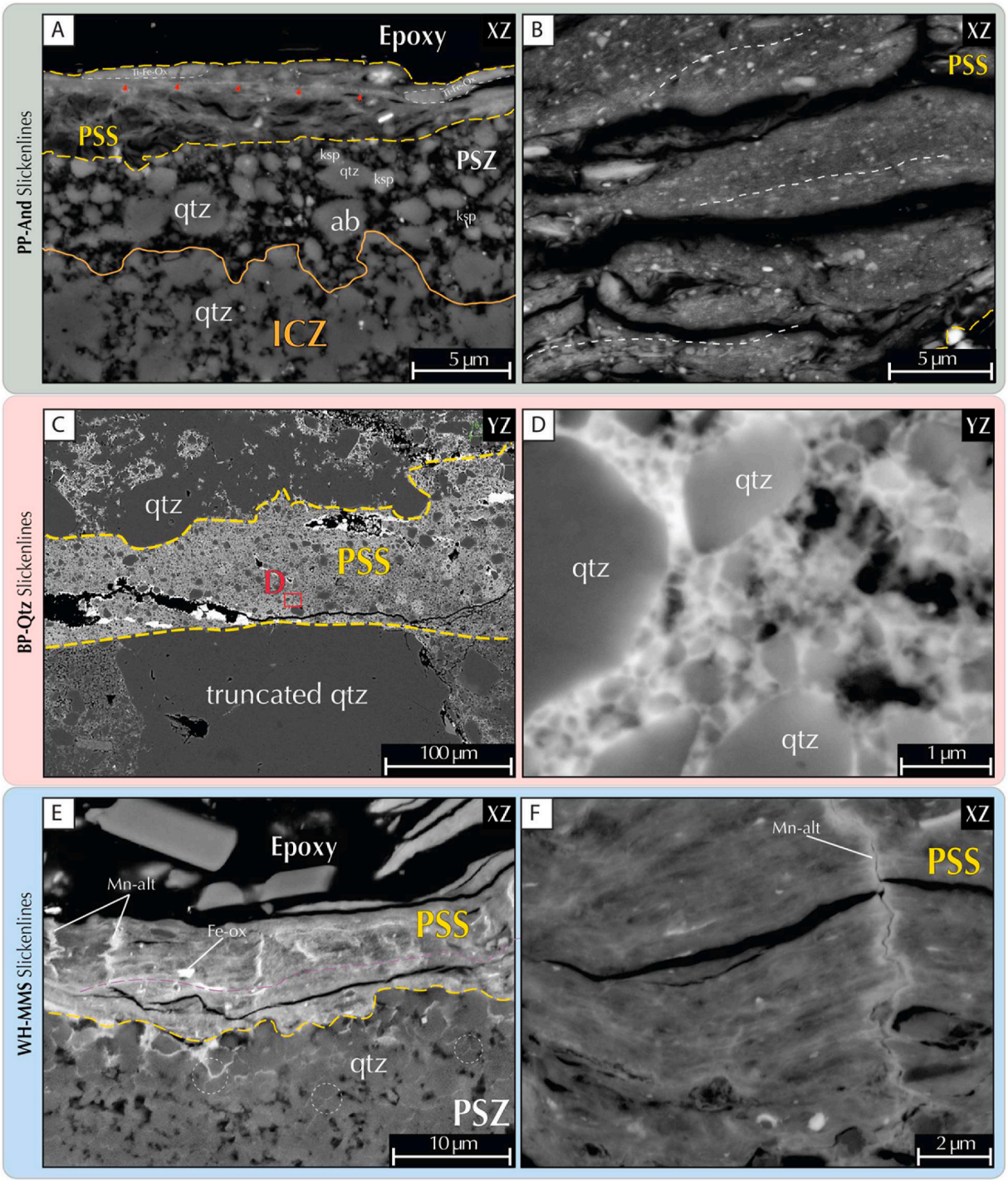

Fig. 10. SEM-BSE images of the Principal Slip Zones. **PP-And slickensides:** A-B) SEM-BSE operated with 20 kV accelerating voltage and 8.0 nA beam current. A) Close-up of PSZ in Fig. 8B.i, showing the presence of a thin PSS and a quartz-rich Increased Cohesion Zone (ICZ) and PSS. Note the PSS is a thin layer (a few microns thick) comprising a randomly oriented Al-and Fe-rich "wispy" phyllosilicate-like matrix and submicron sized particles. Note the roundness of most clasts and Fe-rich veinlet in PSS, red arrows. The ICZ is characterized by a decrease in porosity, grains with irregular and serrated grain boundaries, and sintering microstructures. Further detailed close-ups of the ICZ microstructures are shown in Fig. A6. B) Close-up of dense region of PSS. Note the presence of rounded nano-sized particles and elongated preferentially oriented grains, highlighted by white dashed lines. **BP-Qtz slickensides:** C) Close-up of the PSS from Fig. 8D.ii. Image shows a sharp decrease in grain size from the PSZ (outside of the yellow boundary) towards the PSS, which is characterized by a Fe-oxide-rich layer of micron-sized grains supported in a fine grain matrix. Note truncation of quartz clast by the PSS. D) Close-up of PSS matrix shows matrix comprises predominantly submicron-sized qtz grains and Fe-ox cement (bright colors). Note roundness and lack of fractures on matrix grains and euhedral growth of Fe-oxide blades into void spaces. **WH-MMS slickensides:** E) Close-up into the PSS Fig. 8F.iii, shows it comprises a dense layered matrix with rounded grains and preferentially oriented elongated grains. Bright vertical features correspond to areas enriched in Mn. Layering is highlighted by a magenta dotted line. Note interstitial spaces in PSZ are decorated by bright material, highlighting grain boundaries (dotted white circles). See Fig. A10 for more details of the interlocked grain boundaries within the PSZ. F) Close-up of PSS. Note dense matrix with little to no porosity and sub-micron rounded grains. (For interpretation of the references to color in this figure legend, the reader is referred to the Web version of this article.)

observed that at the lower grain size range (less than 100 nm), the distributions start to plateau as the grain size approaches the resolution limit of the SEM (a single pixel at the highest magnification equals 0.77 nm). The smallest grain sizes are found within the unconsolidated gouge with an equivalent $d_{min} = 18$ nm, whereas the smallest observable grains within the matrix of the PSS corresponded to 30 nm.

In contrast to the BP-Qtz sample, the PP-And slickenside exhibits two distinct parts that can be discriminated by a break in the GSD slope. Two *D*-values are obtained: a lower, $D_{<} = 2.05 \pm 0.19$ for small grain sizes ($d < d_k$), and $D_{>} = 2.72 \pm 0.06$, for large grain sizes ($d > d_k$), where $d_{k.} \approx 2\ \mu m$ and is the grain size at the intersection of the two curve fits. This intersection (d_k) occurs where grains measured only in the PSS and PSZ overlap. Within the small grain size range, the smallest grains are found embedded within the PSS matrix with a $d_{min} = 30$ nm.

4. Discussion

This work provides a detailed study of surface roughness of slickensides and the associated microstructures in the surrounding fault rocks from three different fault zones hosted in various rock types and formed under different tectonic settings. The observations from both the surface and respective volume and their implications for our understanding of faulting processes are discussed below.

4.1. Fault surface roughness analyses

Fully characterizing a fault surface is of particular importance for better understanding fault processes. It has been shown that the stress distribution is affected by fault geometry, as the latter controls to a first degree the real contact area (e.g., Ben-Zion and Rice, 1997; Bruhat et al., 2020; Cattania and Segall, 2021; Harbord et al., 2017; Sagy and Lyakhovsky, 2019; Tal et al., 2020). Our current understanding of fault surface geometry is that it is self-affine and that it can be characterized by four parameters (H_{per}, H_{par}, C_{par}, C_{per}) (Brodsky et al., 2016; Candela et al., 2009, 2012). In agreement with other reports, our studied fault surfaces further indicate that regardless of lithology or tectonic setting, the roughness of individual fault surfaces exhibits an anisotropic self-affine topography with Hurst exponents (*H*) and pre-factors (*C*) within the *0.4-0.8* range and 10^{-5} - 10^{-2}, respectively. The surface roughness of our samples, however, consistently exhibited slightly smaller H_{per}-values and less anisotropy than most reported natural fault surfaces (Table 1), i.e., the roughness measured parallel- and perpendicular to the slip lineations exhibited closely valued Hurst exponents with mean $H_{par} = 0.53 \pm 0.07$ and $H_{per} = 0.60 \pm 0.10$ within error to the more commonly reported $H_{par} \approx 0.6$ and $H_{per} \approx 0.8$, (Bistacchi et al., 2011; Candela et al., 2009, 2012; Power and Tullis, 1989; Renard et al., 2012; Sagy et al., 2007; Thom et al., 2017; Tisato et al., 2012).

In addition to describing fault surface geometry via fractal descriptors (H_{per}, H_{par}, C_{par}, C_{per}), this work includes multiscale analyses (MSA) on the height distribution of fault surfaces. Our results suggest the kurtosis and skewness of such distributions deviate from Gaussian with a noticeable dependence on the scale of observation, which contrast to some of the models used in earthquake simulations that typically assume faults as Gaussian self-affine rough surfaces (e.g., (Cattania and Segall, 2021; Graves and Pitarka, 2016). The latter has important implications on our understanding of the role of geometry in faulting processes, as studies on the contact behavior of non-Gaussian surfaces have reported that roughness parameters skewness and kurtosis correlate to noticeable effects on tribological properties such as: friction, wear, mean asperity pressure, and contact area (Ghosh and Sadeghi, 2015; Gu et al., 2021; Kim et al., 2006; Kotwal and Bhushan, 1996; McCool, 1992; Sedlaček et al., 2012; Tayebi and Polycarpou, 2004; Tomota et al., 2019; W.-Z. Wang et al., 2006; Yan et al., 2014; S. S. Zhang et al., 2014) and fluid transport properties (M. Wang et al., 2016). Thus, further measurements of fault surfaces that also characterizes the distribution of their heights in addition to their fractality seem crucial for more accurate representations of fault roughness in models that explore the role of geometry on seismic slip.

4.2. Microstructures under fault surfaces

While this simplification of fault zones into self-affine rough surfaces is useful for making educated predictions of fault surface geometry at scales and locations not accessible with the current technology (subsurface faults), it is worth noting that wear and therefore slip on a fault cannot be entirely explained by two rough surfaces sliding past each other. Firstly, microstructural observations near single fault surfaces have reported the presence of a discrete zone that concentrates strain and wear comprising extremely comminuted layers with an abundance of nanoparticles and/or other types of tribofilms within the PSZ and PSS (Ault et al., 2019; De Paola, 2013; Dor and Reches, 2005; Goldberg et al., 2016; Heesakkers et al., 2011; Houser et al., 2021; Kuo et al., 2016; McDermott et al., 2017; Odlum et al., 2022; Ohl et al., 2020; Otsubo et al., 2013; Pec et al., 2016; Power and Tullis, 1989; Rowe et al., 2019; Shervais and Kirkpatrick, 2016; Siman-Tov et al., 2013, 2015; Taylor et al., 2021; Tisato et al., 2012; Verberne et al., 2014, 2019; Viti et al., 2016), suggesting that individual fault surface evolution and wear could be better modeled by what is known in tribology as third-body wear (Boneh et al., 2014; Boneh and Reches, 2018; Brodsky et al., 2020; Milanese et al., 2019). More importantly, however, geologic and experimental observations from the submillimeter to kilometers scale indicate that fault zones involve the interaction several structures, with multiple anastomosing fault strands occasionally crosscutting each other (Faulkner et al., 2003; Rowe et al., 2018; Shervais and Kirkpatrick, 2016; Swanson, 1988; Torabi et al., 2020, 2021).

For instance, observations of individual natural slickensides and their respective host rocks reveal an intricate set of structures that document progressive localization of strain into what eventually become multiple principal slip surfaces on which subsequent sliding takes place. Specifically, most samples exhibited foliated cataclasites with S–C-like fabrics, with clasts progressively becoming finer toward the C-plane-parallel principal slip surfaces as documented in Fig. 9, similar to the structures reported along the PSS of numerous other fault zones (Berthé et al., 1979; Hippertt, 1999; Jordan, 1987; Kirkpatrick and Brodsky, 2014; Y.-J. Lee, 1991; A. Lin, 2001; S. Lin et al., 2007; S. Lin and Williams, 1992; Nakamura and Nagahama, 2002; Ortega-Arroyo, 2017). Such observations suggest that development of the PSS is preceded by formation of progressively mechanically weaker zones along which strain is further localized. Grain size reduction can lead to a strong localized weakening when particles reach nanometric sizes associated with significant changes in rheological behavior (e.g. Sun and Pec 2021). A simple sequential model is proposed in Fig. 13 based on the observations from natural slickenside samples, analogue experiments with no pre-cut fault surfaces (Will and Wilson, 1989; C. J. L. Wilson and Will, 1990) and numerical modeling (Finch et al., 2020). Therefore, in our interpretation the exposed slip surfaces are the end product of fault slip and wear on fault zone and not the initial conditions on which slip initiate. Furthermore, the geometry of the PSZ boundary with host rock appears to follow the underlying structure by exploiting the S-, C- or C′-planes (Fig. 9).

At low to intermediate strain, deformation is accommodated via incremental development of oriented fabrics along S–C structures, as shown in Fig. 13B (Will and Wilson, 1989; C. J. L. Wilson and Will, 1990). At higher strains, passive rotation of S-planes into C-planes (Fig. 13C) becomes a more efficient way to accommodate strain over creation of new planes, (Berthé et al., 1979; Finch et al., 2020; Hippertt, 1999; Jordan, 1987), which create rheologically weaker regions that accommodate higher strain rates (Finch et al., 2020) and can progressively link with each other to form through going shear zones (Finch et al., 2020; Pec et al., 2016; Will and Wilson, 1989; C. J. L. Wilson and Will, 1990), as sketched on Fig. 13D, akin to the process zone suggested by (Cox and Scholz, 1988). The development of these through going

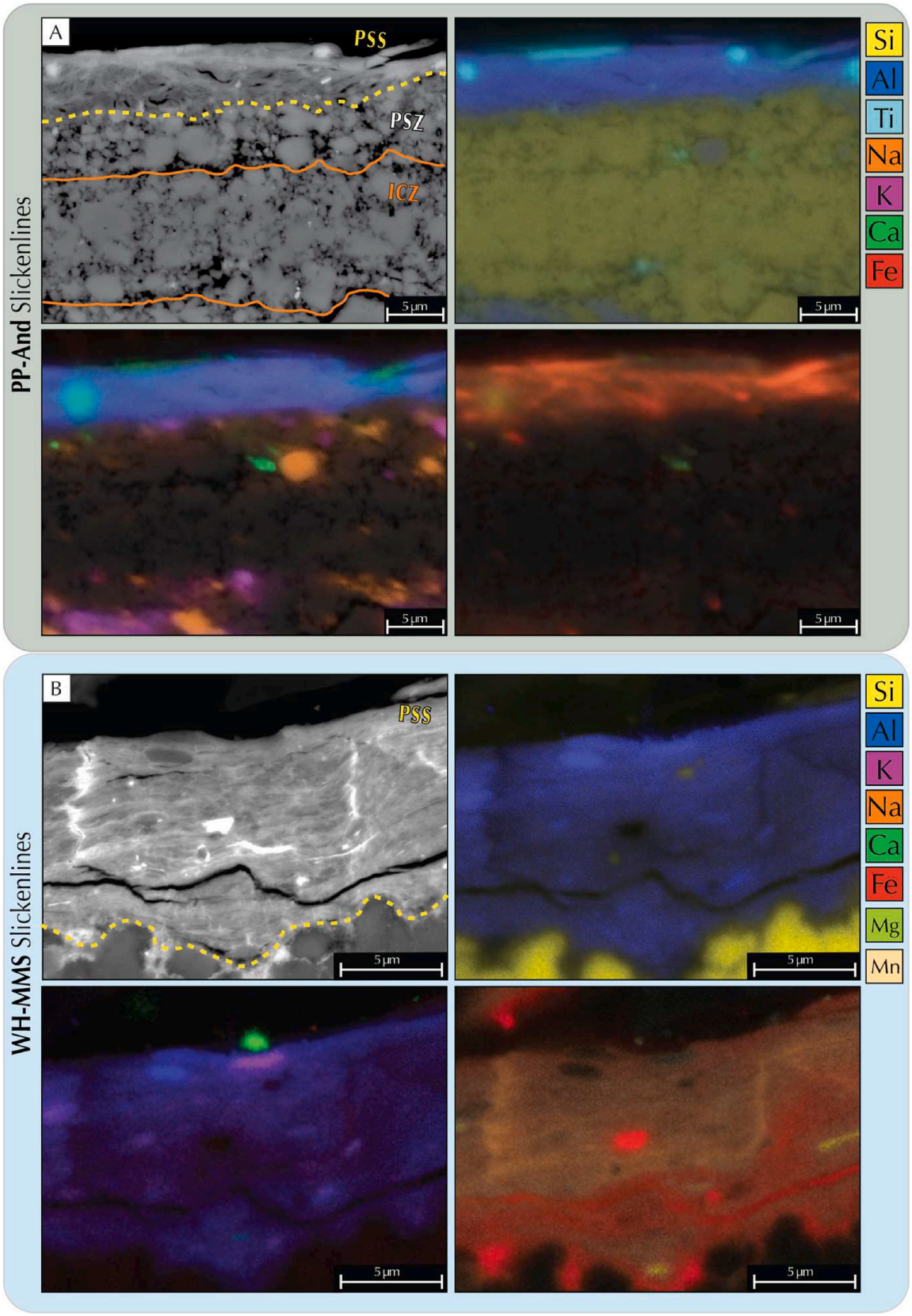

Fig. 11. Compositional EDS maps of Principal Slip Surfaces. A) PP-And slickenside: from Fig. 10A Note Si-rich (quartz) Increased Cohesion Zone (ICZ) and Al, Fe and Ti enriched PSS. B) WH-MMS slickensides: Close-up of PSS in Fig. 10E showing PSS is enriched in Al, Fe. Bright fractures enriched in Mn. Note thin Al-, K-, and Mg-rich rods preferentially aligned subparallel to the slip surface. Note: SEM-EDS was operated with a beam current of 8 nA and a 20 kV accelerating voltage.

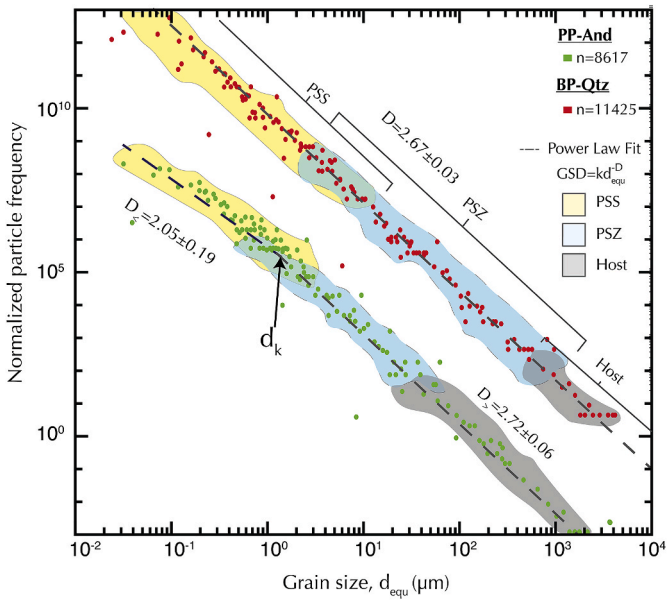

Fig. 12. Grain Size Distributions of BP-Qtz (red) and PP-And (green) host rocks. Data has been displaced vertically for clarity. The GSD of quartzite samples can be described by a single $D = 2.67 \pm 0.03$, whereas GSD has two distinct slopes for $D_{<} = 2.05 \pm 0.19$ and $D_{>} = 2.72 \pm 0.06$ for grain size smaller or larger than $d_k \approx 2$ μm, respectively. The different color envelopes indicate the range of grain sizes found within the PSS, PSZ, and the host rock. Data points outside the color envelopes correspond to artifacts due to the limited resolution in each measured image. (For interpretation of the references to color in this figure legend, the reader is referred to the Web version of this article.)

shear zones initiated by interlinking segments of the previously formed S-, C-and C′- planes, which could explain the geometry of the PSZ-host rock boundary that we observed in many of our samples (Fig. 9). The growth of these localized interlinked shear zones also facilitates infiltration of fluids, as seen in the ubiquitous concentration of secondary minerals and/or alteration products (mainly Fe-ox) along the PSZ and PSS (Figs. 8–11) that likely cause further weakening and slip due to metasomatic reactions, pore pressure effects and grain size reduction (e.g., Calzolari et al., 2020). The latter suggests an extreme degree of strain localization, where most of the deformation is accommodated by extreme comminution along thin kinematically favorable regions, generally a few tens of microns thick, as documented in Figs. 8–10.

4.3. Extreme comminution along principal slip zones

To better characterize the extreme comminution processes affecting our samples we performed grain size analyses. Interestingly, the way the grain sizes are distributed appears to vary between the PP-And and the BP-Qtz samples. For instance, the slickenside within the BP-Qtz sample shows a GSD that can be described with a single D value for over six orders of magnitude, whereas the PP-And GSD has a break in slope near $d_k \approx 2$ μm, Fig. 12. Grain size measurements from other polymineralic natural and experimental fault rocks have also reported a break in the slope of their GSD at similar critical grain sizes d_k that suggest a change in the dominant comminution mechanisms with attrition and shearing becoming more important at values lower than d_k, usually attributed to the grinding limit (Billi and Storti, 2004; F. M. Chester et al., 1993; J. S. Chester et al., 2005; Keulen et al., 2007). Our BP-Qtz sample does not exhibit this transition and contrasts with what Keulen et al. (2007) reported for quartz grains in polymineralic gouges. There could be multiple explanations for the discrepancies at these scales. Firstly, the difference could be related to different breakage mechanisms at sub-micron scale associated to the parent mineralogy (Knieke et al., 2011), as the observations reported in Keulen et al. (2007) were done on granitoid lithologies and ours on quartzite (BP-Qtz) and andesite (PP-And). Moreover, the break in slope observed in the PP-And GSD could be related to changes in material properties likely caused by mechanochemical and/or tribochemical reactions acting along the friction zone, PSS, as the d_k appears at the transition where their grain sizes overlap between the PSZ and PSS (Knieke, 2012; Knieke et al., 2011; Romeis et al., 2016). It is possible that partial mechanical amorphization is among some of the reactions occurring within the PSS, which could help explain the distinct textures observed along the PSS and its GSD. For instance, the dense portion of the PSS, Fig. 10B,E-F, exhibits similar textures to those observed along the silica layer within the slickensides studied by Taylor et al. (2021), wherein Fe-ox nanorods are embedded in a partially amorphous matrix, while the "wispy" microporous matrix, observed in Fig. 10A, resembles the textures reported from hydrothermally altered quenched frictional melts in Fondriest et al. (2020) likely representing portions that have undergone more advanced hydrothermal alteration with formation of clay minerals, (e.g., Fe-smectite, Fig. A4). Furthermore, observations of coeval amorphous and nanocrystalline material are not uncommon along high strain frictional interfaces and have been widely reported along natural

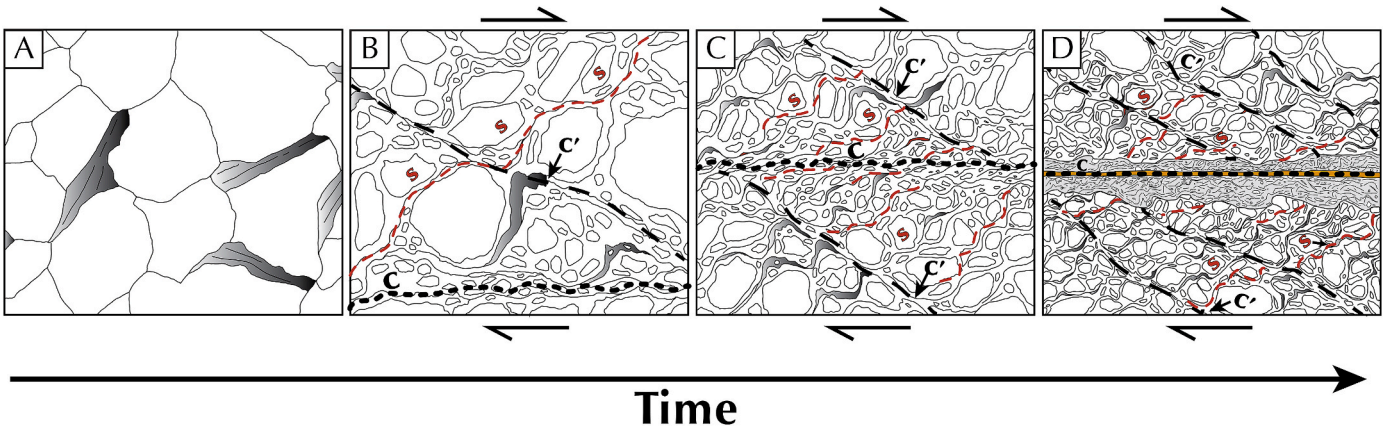

Fig. 13. Schematic sequential model of slickenside development. A) Initial undeformed rock. B) Development of S–C–C′ fabrics at low -intermediate strain levels. S-foliation (red-dashed lines) is defined by asymmetrical clast and clast aggregates with their tails oriented at about 45° to the C-surface (black-dotted lines), whereas C′-shear bands appear oblique orientations (black-dashed lines). C) As shearing continues more S–C′ fabrics propagate throughout the sample and create rheologically weaker regions via grain size reduction that preferentially rotate towards C-planes. Note S-planes become more subparallel towards the C-plane. D) Strain further localizes along the C-planes in the form of finely comminuted material observed in the PSZ (grey) and PSS (yellow). (For interpretation of the references to color in this figure legend, the reader is referred to the Web version of this article.)

fault surfaces (Ault et al., 2019; Houser et al., 2021; Kirkpatrick et al., 2013; Kuo et al., 2016; Ohl et al., 2020; Verberne et al., 2014, 2019; Viti et al., 2016), rock deformation experiments (Kaneki et al., 2020; Marti et al., 2012b, 2016, 2020; Pec et al., 2012a; 2012b; Pec and Al Nasser, 2021; Toy et al., 2017), and deformation of engineering materials (Han et al., 2012; Viat et al., 2017; Y. S. Y. S. Zhang et al., 2014; Zhao et al., 2016), indicating that both nanocrystalline and amorphous material are common products during frictional wear processes regardless of the parent material, and an important component to consider when studying rheology of faults. Nanocrystalline fault rocks are inherently weaker than their microcrystalline counterparts and therefore can form in-situ weak layers along which strain further localizes (Sun and Pec 2021).

Furthermore, based on the microstructure of each sample it is possible that the observed GSD differences relate to different degrees of comminution, as seen from the more pervasively deformed BP-Qtz sample (Figs. 4, 8C-D, and 9A-B) compared to the PP-And sample (Fig. 8A–B, A3 and A5). Previous studies in confined comminution of granular materials using simple Discrete Element and Apollonian gasket models suggest that the GSD continuously shifts as the porosity is reduced until the GSD reaches an ultimate power law that also determines the ultimate contact force distribution (Ben-Nun et al., 2010). Additionally, the difference in GSD also appears to correlate with the measured roughness for the PP-And (Fig. 5A) and BP-Qtz (Fig. 5Bii-iii) samples, i.e., higher proportion of nanometric particles (Fig. 12) correlates with smoother surfaces and smaller H and C values (Table 1). Alternatively, Knieke et al. (2009) work on ultrafine particle (nm-range) production with stirred media mills on a variety of different materials shows that the ultimate size that a particle can be broken into, i.e., grinding limit, depends on a multitude of variables including stressing types, the material of the particles to be milled as well as the size and material of the milling particles, and solvents (e.g., hydrous fluids). Thus, the ultimate particle distribution observed along comminuted rocks could also reflect the conditions during grinding. Lastly, the serrated grain boundaries observed along the ICZ in Fig. 10A and Fig. A6. could indicate that the GSD is also likely overprinted by post deformation fault healing and grain growth (Keulen et al., 2008).

5. Summary and conclusions

We investigated the surface roughness and associated microstructures of natural slickenside samples exposed along minor slip surfaces from three different fault systems hosted in andesite, quartzite and mylonitic meta-sedimentary lithologies. We found that in addition to exhibiting the usually reported self-affine roughness, with mean $H_{par} = 0.53 \pm 0.07$ and $H_{per} = 0.60 \pm 0.10$, all surfaces exhibited non-Gaussian height distributions with noticeable scale-dependence on their S_{kur} and S_{sk} roughness parameters. While our dataset is limited to the shorter length scales associated with fault surface roughness ($\leq 10^{-2}$ m), further studies at larger scales could help constrain the type of height distributions common to natural faults. Moreover, our microstructural analyses suggest such surfaces are likely the product of progressive strain localization and partitioning along regions with high degree of fabric development (S–C–C′- fabrics) that culminate in multiple principal slip zones throughout the samples identified by a sharp decrease in clast size and thin ($\leq$100 μm) principal slip surfaces wherein nanosized particles are abundant along with other tribofilms and reaction products. The prevalence of nanoparticles observed within fault zones regardless of lithology or tectonic setting urges the need to investigate the effect of nanogranular material on the rheological and frictional properties of faults.

CRediT authorship contribution statement

Daniel Ortega-Arroyo: Conceptualization, Data curation, Formal analysis, Investigation, Methodology, Writing – original draft, Writing – review & editing. **Matěj Peč:** Writing – review & editing, Supervision, Funding acquisition.

Declaration of competing interest

The authors declare that they have no known competing financial interests or personal relationships that could have appeared to influence the work reported in this paper.

Data availability

I have shared the link to my data in the Data Availavility Statement section of the manuscript

Acknowledgments

Funding for the CORD technician support from NSF # 1833478, funding by the J.H. and E.V. Wade Fund from Massachusetts Institute of Technology (MIT) research support committee and MIT's MISTI fund # 1380265 is gratefully acknowledged. We would also like to acknowledge the staff at the Materials Research Science and Engineering Centers at MIT for their help with their ZEISS Merlin HR-SEM and Rüdiger Killian and his lab at the Martin-Luther-Universität Halle for their help with the Bruker Tornado μ-XRF spectrometer.

We would also like to thank Christie Rowe and McGill University, who allowed us to join their 2019 field course and collect the Waterman Hill samples, Oliver Jagoutz and the MIT-EAPS 2020 field course for allowing us to collect the Big Piute samples, and Juan Ignacio Arroyo Verástegui, who helped me collect the sample from Falla de Plan de los Plátanos.

7 Appendix

7.1 Sampling criteria

We focused our sampling of slickensides to minor faults in the damage zone of three different fault system (PP-And, BP-Qtz, and WH-MMS) that exhibited relatively intact surfaces (no observables notches or scratches). We collected the most pristine regions where the specularly reflective patches were preserved or as mentioned in the sampling section of the manuscript, collected areas that preserved both sides of the fault as shown in Fig. A1.

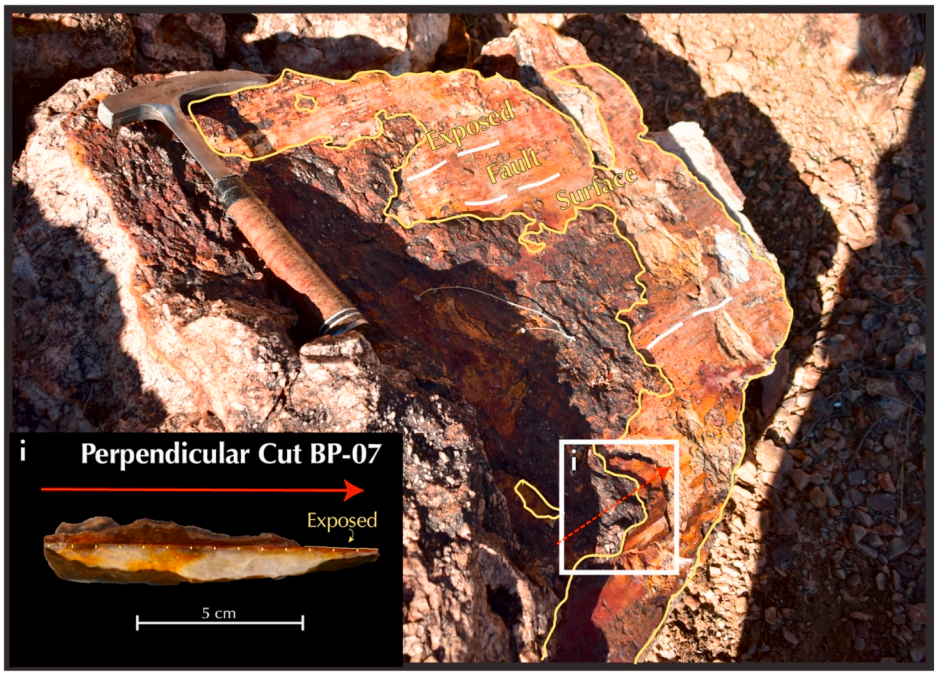

Fig. A1. Sampling of slickensides that contain both sides of fault surface. Yellow line highlights the exposed slickenside surface. White square corresponds to the collected sample that contains both exposed and covered fault surface. Hammer for scale (33.02 cm long). Inset shows collected sample cut perpendicularly to the slip surface and parallel to slip direction (red arrow). Small yellow arrows indicate principal slip surface continues throughout the covered section of the sample.

7.2 Evaluation of signal processing technique

The accuracy of the signal processing technique was assessed by recording the difference between the "input" Hurst exponents of randomly generated synthetic isotropic self-affine surfaces using the code provided in Candela et al. (2009) and the "output" recovered with our methods. For each value of the input Hurst exponent, we analyzed a set of 1000 synthetically generated surfaces as presented in Fig. A1. We further assessed our method by analyzing surface data from the Corona Heights fault surface samples from Thom et al. (2017). The average Hurst exponents of the Corona Heights Fault slickenside samples corresponded to 0.72 ±. 0.11 and 0.78 ± 0.09 for the parallel and perpendicular orientations, respectively. However, when the data in both directions are considered, we obtained 0.75 ± 0.10, which agrees with the value found by Thom et al. (2017).

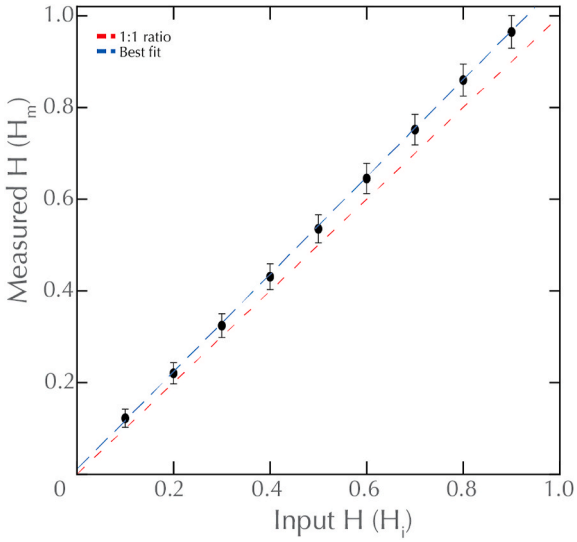

Fig. A2. Calibration of PSD method for calculating the Hurst exponent (*H*). Note that the measured Hurst exponent (H_m) does not follow a one-to-one ratio (red). Instead, it has a linear best fit of the form $H_m = 1.065\ H_i + 0.006$ with a coefficient of determination $R^2 = 0.999$.

Table A1
Number of profiles averaged per surface to estimate Hurst (*H*) and Pre-exponent (*C*)

Sample	Fault	n_{par} [a]	n_{per} [b]
AU-01	PP-And	5646	4600
BP-04	BP-Qtz	4593	2956
BP-07a	BP-Qtz	1601	1601
BP-07b	BP-Qtz	2903	3879
WH-3a-1	WH-MMS	6751	4251
WH-3a-2	WH-MMS	5046	3925
WH-3c	WH-MMS	4323	3115
WH-3d	WH-MMS	4502	3038

[a] Number of profiles parallel to lineations averaged for H_{par} and C_{par}.
[b] Number of profiles perpendicular to lineations averaged for H_{per} and C_{per}.

7.3 Additional microstructures

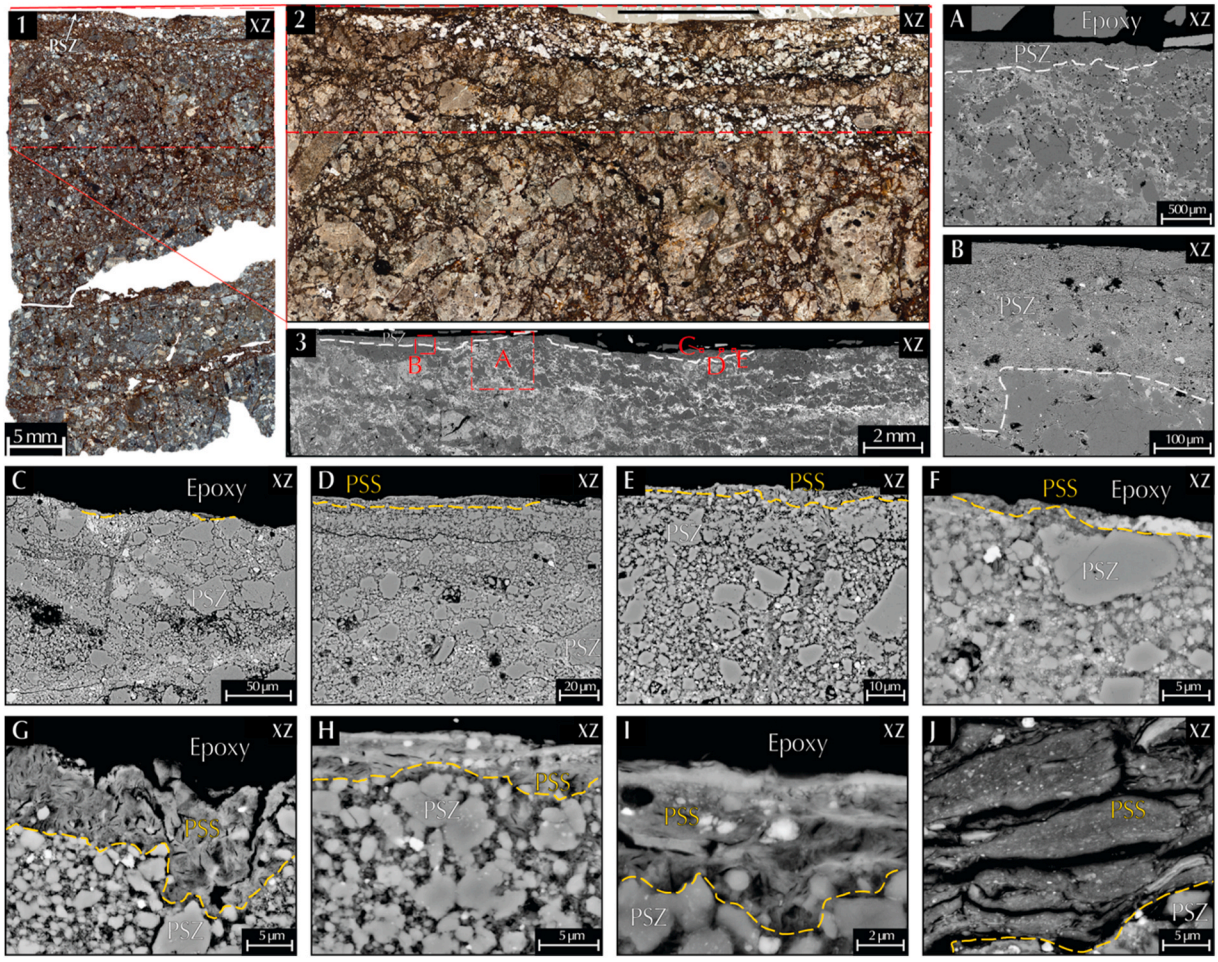

Fig. A3. Set of images at progressively higher magnifications used in the GSD determination of PP-And slickenside. See text for details.

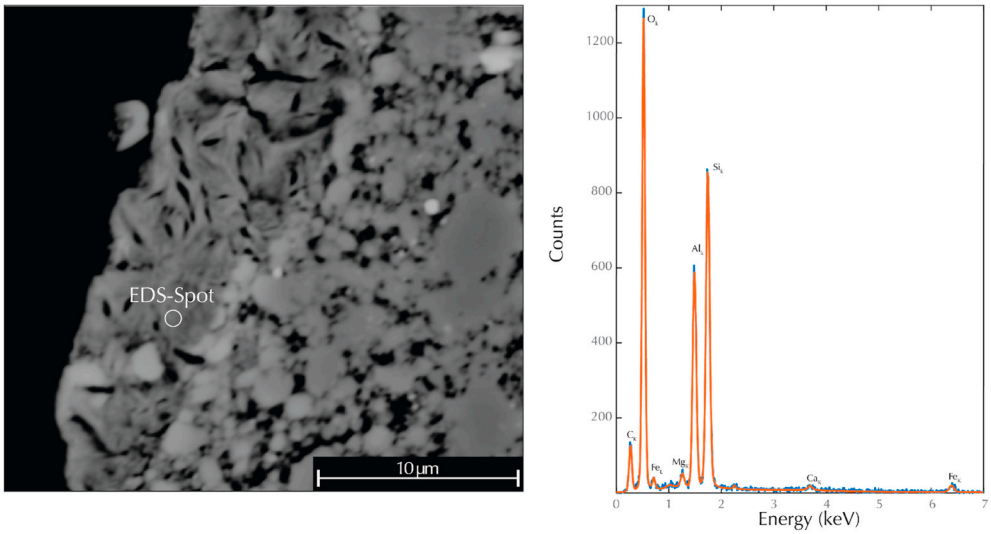

Fig. A4. EDS-spectrum of "wispy" PSS from PP-And slickenside. Note: SEM was operated with a beam current of 8 nA and a 20 kV accelerating voltage

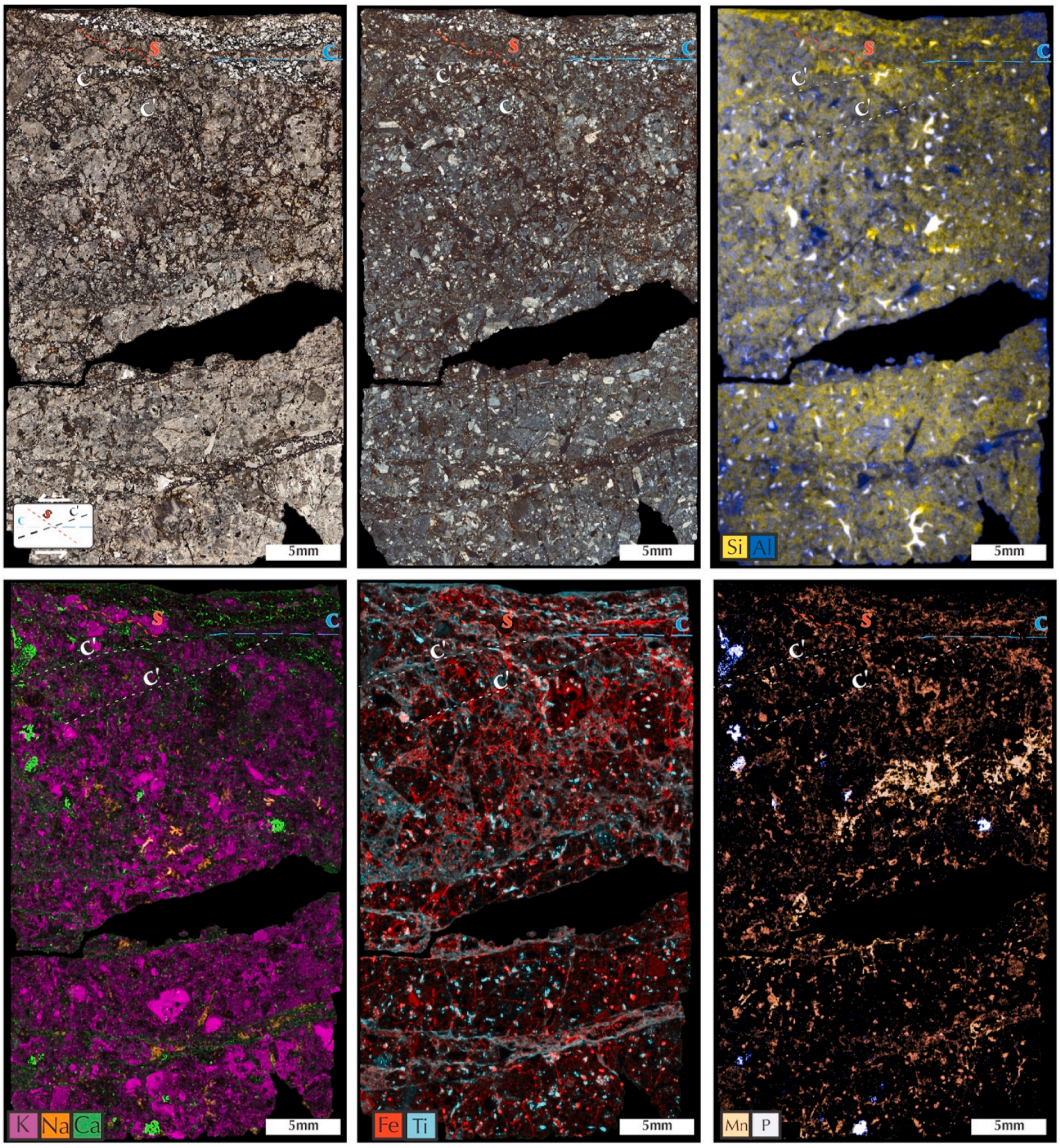

Fig. A5. XRF compositional maps of PP-And sample shown in Fig. 8A. Note Ti-rich regions highlight slip surfaces and S–C′ fabrics. Note images are mirrored compared to

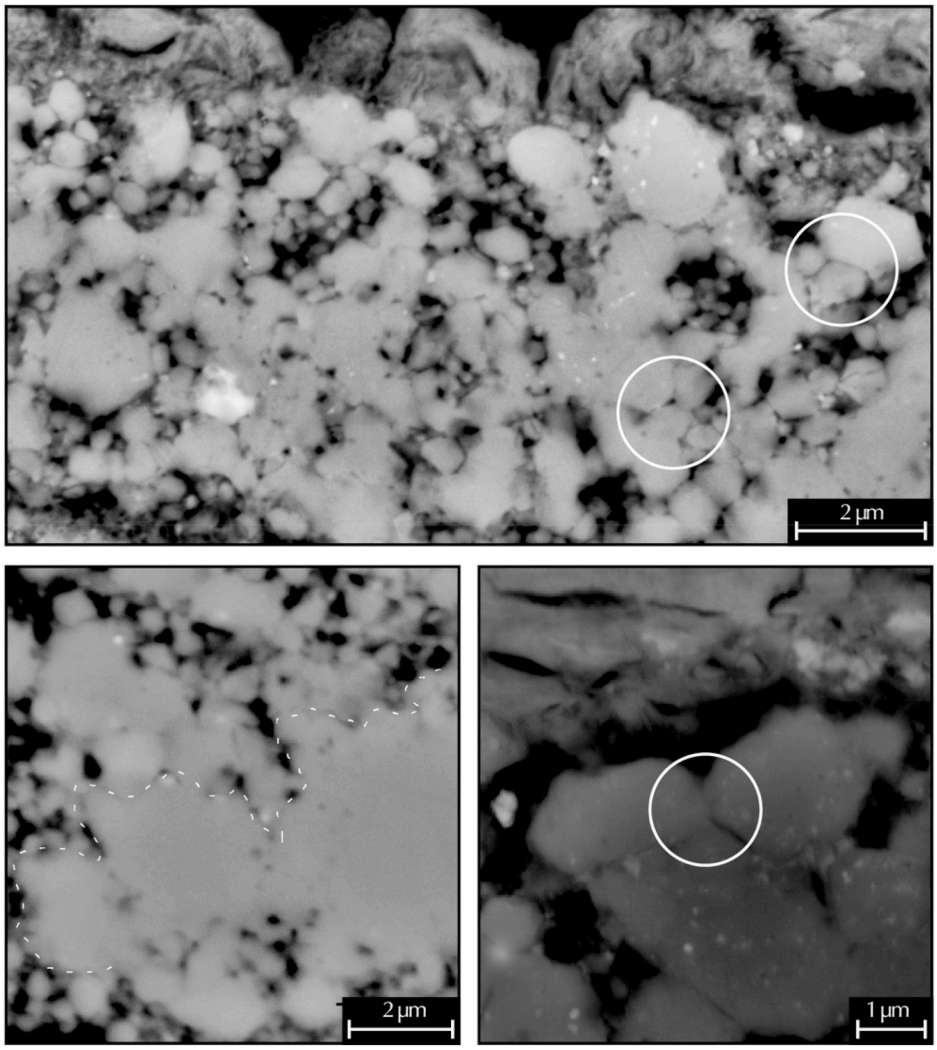

Fig. A6. SEM BSE photomicrographs of the ICZ from the PP-And slickenside showing grains with irregular and serrated grain boundaries (dotted white line), and sintering microstructures along with triple junctions (white circles).

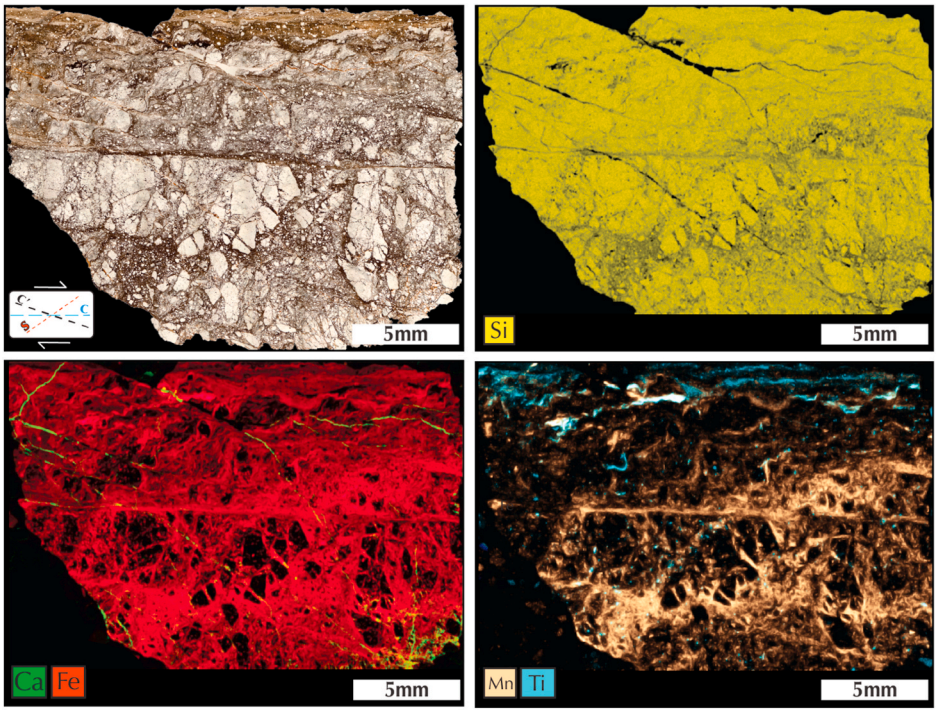

Fig. A7. XRF compositional maps of BP-Qtz sample shown in Fig. 9B. Note that higher concentration of Ti highlights areas near the principal slip zone (top of image).

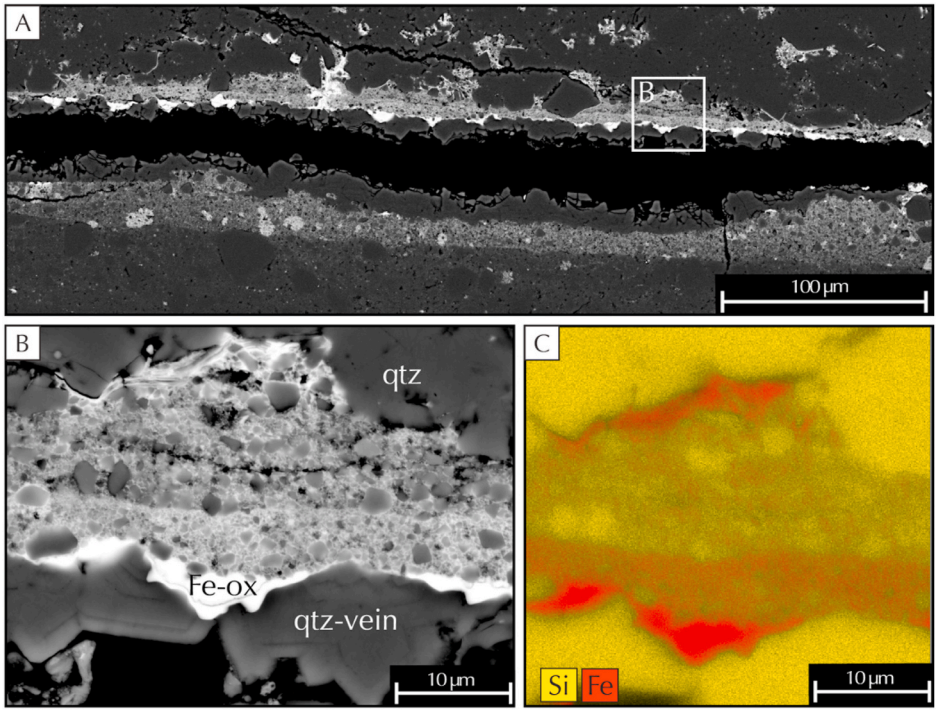

Fig. A8. SEM-BSE photomicrographs of the PSS in BP-Qtz. A) Open fracture with Fe-ox and secondary quartz fracture fill. B) Close up into PSS with Fe-ox and quartz fracture fill. C) EDS compositional map

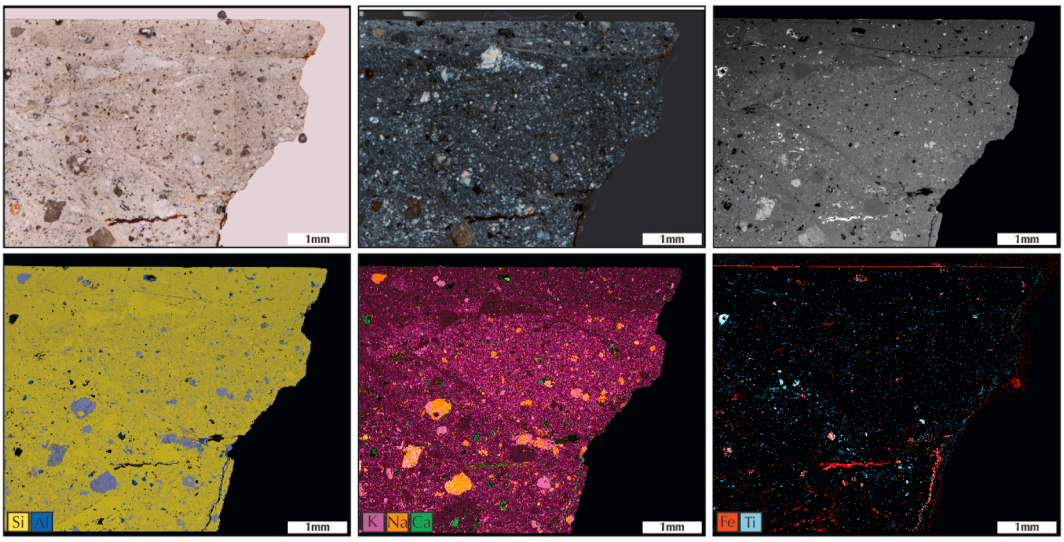

Fig. A9. SEM- EDS compositional map of sample shown in Fig. 9D. Note Fe-rich region at the top of the sample highlights the principal slip surface. SEM was operated with a beam current of 8 nA and a 20 kV accelerating voltage

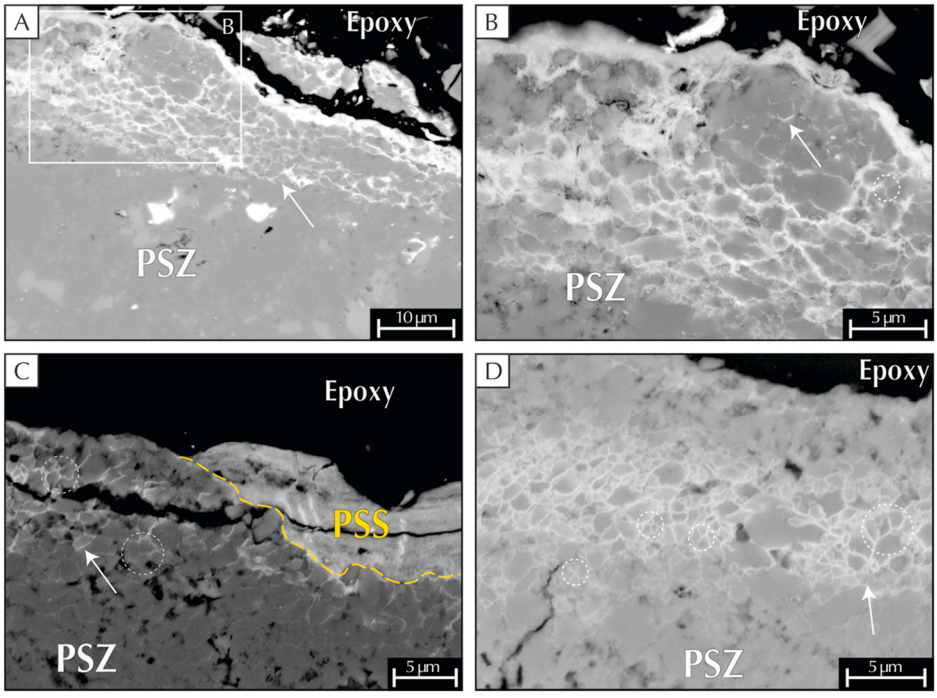

Fig. A10. SEM- BSE photomicrographs of WH-MMS slickensides near PSS shown in Fig. 10E–D, showing interlocked grain boundaries highlighted by bright material (white arrow) and triple junctions (dotted white circles) within the PSZ.

References

Ault, A.K., Jensen, J.L., McDermott, R.G., Shen, F.-A., Van Devener, B.R., 2019. Nanoscale evidence for temperature-induced transient rheology and postseismic fault healing. Geology 47 (12), 1203–1207. https://doi.org/10.1130/G46317.1.

Ben-Nun, O., Einav, I., Tordesillas, A., 2010. Force attractor in confined comminution of granular materials. Phys. Rev. Lett. 104 (10), 108001 https://doi.org/10.1103/PhysRevLett.104.108001.

Ben-Zion, Y., Rice, J.R., 1997. Dynamic simulations of slip on a smooth fault in an elastic solid. J. Geophys. Res. 102 (B8), 17771–17784. https://doi.org/10.1029/97jb01341.

Berthé, D., Choukroune, P., Jegouzo, P., 1979. Orthogneiss, mylonite and non coaxial deformation of granites: the example of the South Armorican Shear Zone. J. Struct. Geol. 1 (1), 31–42. https://doi.org/10.1016/0191-8141(79)90019-1.

Bhushan, B., 2013. Introduction to Tribology. John Wiley & Sons. Retrieved from. https://play.google.com/store/books/details?id=b0nhJrqsoZ0C.

Billi, A., Storti, F., 2004. Fractal distribution of particle size in carbonate cataclastic rocks from the core of a regional strike-slip fault zone. Tectonophysics 384 (1), 115–128. https://doi.org/10.1016/j.tecto.2004.03.015.

Bistacchi, A., Griffith, W.A., Smith, S.A.F., Di Toro, G., Jones, R., Nielsen, S., 2011. fault roughness at seismogenic depths from LIDAR and photogrammetric analysis. Pure Appl. Geophys. 168 (12), 2345–2363. https://doi.org/10.1007/s00024-011-0301-7.

Boneh, Y., Reches, Z., 2018. Geotribology - friction, wear, and lubrication of faults. Tectonophysics 733, 171–181. https://doi.org/10.1016/j.tecto.2017.11.022.

Boneh, Y., Chang, J.C., Lockner, D.A., Reches, Z., 2014. Evolution of wear and friction along experimental faults. Pure Appl. Geophys. 171 (11), 3125–3141. https://doi.org/10.1007/s00024-014-0801-3.

Bowden, F.P., Tabor, D., Taylor, G.I., 1939. The area of contact between stationary and moving surfaces. Proc. Roy. Soc. Lond. Math. Phys. Sci. 169 (938), 391–413. https://doi.org/10.1098/rspa.1939.0005.

Brodsky, E.E., Kirkpatrick, J.D., Candela, T., 2016. Constraints from fault roughness on the scale-dependent strength of rocks. Geology 44 (1), 19–22. https://doi.org/10.1130/G37206.1.

Brodsky, E.E., McLaskey, G.C., Ke, C.-Y., 2020. Groove generation and coalescence on a large-scale laboratory fault. AGU Advances 1 (4). https://doi.org/10.1029/2020av000184.

Brown, C.A., Hansen, H.N., Jiang, X.J., Blateyron, F., Berglund, J., Senin, N., et al., 2018. Multiscale analyses and characterizations of surface topographies. CIRP Annals 67 (2), 839–862. https://doi.org/10.1016/j.cirp.2018.06.001.

Brown, S.R., Scholz, C.H., 1985. Broad bandwidth study of the topography of natural rock surfaces. J. Geophys. Res. 90 (B14), 12575 https://doi.org/10.1029/jb090ib14p12575.

Bruhat, L., Klinger, Y., Vallage, A., Dunham, E.M., 2020. Influence of fault roughness on surface displacement: from numerical simulations to coseismic slip distributions. Geophys. J. Int. 220 (3), 1857–1877. https://doi.org/10.1093/gji/ggz545.

Caine, J.S., Evans, J.P., Forster, C.B., 1996. Fault zone architecture and permeability structure. Geology 24 (11), 1025–1028. https://doi.org/10.1130/0091-7613(1996)024<1025:FZAAPS>2.3.CO;2.

Calzolari, G., Ault, A.K., Hirth, G., McDermott, R.G., 2020. Hematite (U-Th)/He thermochronometry detects asperity flash heating during laboratory earthquakes. Geology 48 (5), 514–518. https://doi.org/10.1130/G46965.1.

Candela, T., Renard, F., Bouchon, M., Brouste, A., Marsan, D., Schmittbuhl, J., Voisin, C., 2009. Characterization of fault roughness at various scales: implications of three-dimensional high resolution topography measurements. Pure Appl. Geophys. 166 (10), 1817–1851. https://doi.org/10.1007/s00024-009-0521-2.

Candela, T., Renard, F., Klinger, Y., Mair, K., Schmittbuhl, J., Brodsky, E.E., 2012. Roughness of fault surfaces over nine decades of length scales. J. Geophys. Res. 117 (B8) https://doi.org/10.1029/2011jb009041.

Cattania, C., Segall, P., 2021. Precursory slow slip and foreshocks on rough faults. J. Geophys. Res. Solid Earth 126 (4). https://doi.org/10.1029/2020jb020430.

Chen, J., Verberne, B.A., Niemeijer, A.R., 2020. Flow-to-Friction transition in simulated calcite gouge: experiments and microphysical modeling. J. Geophys. Res. Solid Earth 125 (11), e2020JB019970. https://doi.org/10.1029/2020JB019970.

Chen, X., Madden, A.S., Bickmore, B.R., Reches, Z., 2013. Dynamic weakening by nanoscale smoothing during high-velocity fault slip. Geology 41 (7), 739–742. https://doi.org/10.1130/G34169.1.

Chester, F.M., Logan, J.M., 1986. Implications for mechanical properties of brittle faults from observations of the Punchbowl fault zone, California. Pure Appl. Geophys. 124 (1), 79–106. https://doi.org/10.1007/BF00875720.

Chester, F.M., Friedman, M., Logan, J.M., 1985. Foliated cataclasites. Tectonophysics 111 (1), 139–146. https://doi.org/10.1016/0040-1951(85)90071-X.

Chester, F.M., Evans, J.P., Biegel, R.L., 1993. Internal structure and weakening mechanisms of the san andreas fault. J. Geophys. Res. 98 (B1), 771–786. https://doi.org/10.1029/92jb01866.

Chester, J.S., Chester, F.M., Kronenberg, A.K., 2005. Fracture surface energy of the Punchbowl fault, San Andreas system. Nature 437 (7055), 133–136. https://doi.org/10.1038/nature03942.

Chu, S.X., Tsai, V.C., Trugman, D.T., Hirth, G., 2021. Fault interactions enhance high-frequency earthquake radiation. Geophys. Res. Lett. 48 (20) https://doi.org/10.1029/2021gl095271.

Cox, S.J.D., Scholz, C.H., 1988. On the formation and growth of faults: an experimental study. J. Struct. Geol. Retrieved from https://www.sciencedirect.com/science/article/pii/0191814188900193.

De la Teja Segura, M.Á., Roque Ayala, A., 2007. In: Mexicano, S.G. (Ed.), Carta Geológica-Minera Autlán de Navarro E13-B12 Jalisco, Pachuca, HGO, Mexico : Servicio Geológico Mexicano. Retrieved from. http://mapserver.sgm.gob.mx/Cartas_Online/geologia/956_E13-B12_GM.pdf.

De Paola, N., 2013. Nano-powder coating can make fault surfaces smooth and shiny: implications for fault mechanics? Geology 41 (6), 719–720. https://doi.org/10.1130/focus062013.1.

Di Toro, G., Han, R., Hirose, T., De Paola, N., Nielsen, S., Mizoguchi, K., et al., 2011. Fault lubrication during earthquakes. Nature 471 (7339), 494–498. https://doi.org/10.1038/nature09838.

Dieterich, J.H., Kilgore, B.D., 1996. Imaging surface contacts: power law contact distributions and contact stresses in quartz, calcite, glass and acrylic plastic. Tectonophysics 256 (1), 219–239. https://doi.org/10.1016/0040-1951(95)00165-4.

Doblas, M., 1998. Slickenside kinematic indicators. Tectonophysics 295 (1), 187–197. https://doi.org/10.1016/S0040-1951(98)00120-6.

Dor, O., Reches, Z., 2005. Analysis of Fault Zones Associated with Large Earthquakes in South African Gold Mines. Earth Sciences Institute, Hebrew University, Jerusalem, Israel. Retrieved from. http://earthquakes.ou.edu/nelsam/fault_zones.pdf.

Faulkner, D.R., Lewis, A.C., Rutter, E.H., 2003. On the internal structure and mechanics of large strike-slip fault zones: field observations of the Carboneras fault in southeastern Spain. Tectonophysics 367 (3), 235–251. https://doi.org/10.1016/S0040-1951(03)00134-3.

Faulkner, D.R., Jackson, C.A.L., Lunn, R.J., Schlische, R.W., Shipton, Z.K., Wibberley, C. A.J., Withjack, M.O., 2010. A review of recent developments concerning the structure, mechanics and fluid flow properties of fault zones. J. Struct. Geol. 32 (11), 1557–1575. https://doi.org/10.1016/j.jsg.2010.06.009.

Faulkner, D.R., Mitchell, T.M., Jensen, E., Cembrano, J., 2011. Scaling of fault damage zones with displacement and the implications for fault growth processes. J. Geophys. Res. 116 (B5) https://doi.org/10.1029/2010jb007788.

Ferrari, L., Pasquaré, G., Venegas-Salgado, S., Romero-Rios, F., 2000. Geology of the western Mexican volcanic belt and adjacent Sierra Madre Occidental and Jalisco block. In: Cenozoic Tectonics and Volcanism of Mexico. Geological Society of America, pp. 65–83. https://doi.org/10.1130/0-8137-2334-5.65.

Finch, M.A., Bons, P.D., Steinbach, F., Griera, A., Llorens, M.-G., Gomez-Rivas, E., et al., 2020. The ephemeral development of C′ shear bands: a numerical modelling approach. J. Struct. Geol. 139, 104091 https://doi.org/10.1016/j.jsg.2020.104091.

Fletcher, J.M., Karlstrom, K.E., 1990. Late cretaceous ductile deformation, metamorphism and plutonism in the Piute Mountains, eastern Mojave Desert. J. Geophys. Res. 95 (B1), 487. https://doi.org/10.1029/jb095ib01p00487.

Fletcher, J.M., Bendixen, J., Fillmore, R., Walker, J.D., Glazner, A.F., Bartley, J.M., 1999. Geology of the Mitchel Range and Waterman Hills, San Bernardino County, California. Geological society of America. https://doi.org/10.1130/1999-fletcher-watermanhills.

Fleuty, M.J., 1975. Slickensides and slickenlines. Geol. Mag. 112 (3), 319–322. https://doi.org/10.1017/S0016756800047087.

Fondriest, M., Mecklenburgh, J., Passelegue, F.X., Artioli, G., Nestola, F., Spagnuolo, E., et al., 2020. Pseudotachylyte alteration and the rapid fade of earthquake scars from the geological record. Geophys. Res. Lett. 47 (22) https://doi.org/10.1029/2020gl090020.

Gadelmawla, E.S., Koura, M.M., Maksoud, T.M.A., Elewa, I.M., Soliman, H.H., 2002. Roughness parameters. J. Mater. Process. Technol. 123 (1), 133–145. https://doi.org/10.1016/S0924-0136(02)00060-2.

Ghosh, A., Sadeghi, F., 2015. A novel approach to model effects of surface roughness parameters on wear. Wear: Int. J. Sci. Technol. Friction Lubricat. Wear 73–94. https://doi.org/10.1016/j.wear.2015.04.022, 338–339.

Glazner, A.F., Mills, R.D., 2012. Interpreting two-dimensional cuts through broken geologic objects: fractal and non-fractal size distributions. Geosphere 8 (4), 902–914. https://doi.org/10.1130/GES00731.1.

Glazner, A.F., Bartley, J.M., Douglas Walker, J., 1989. Magnitude and significance of Miocene crustal extension in the central Mojave Desert, California. Geology 17 (1), 50–53. https://doi.org/10.1130/0091-7613(1989)017<0050:MASOMC>2.3.CO;2.

Gold, P.O., Behr, W.M., Fletcher, J.M., Rockwell, T.K., Figueiredo, P.M., 2020. Time-invariant late Quaternary slip rates along the Agua Blanca fault, northern Baja California, Mexico. Tectonics 39 (9). https://doi.org/10.1029/2019tc005788.

Goldberg, R., Siman-Tov, S., Emmanuel, S., 2016. Weathering resistance of carbonate fault mirrors promotes rupture localization. Geophys. Res. Lett. https://doi.org/10.1002/2016gl067788.

Graves, R., Pitarka, A., 2016. Kinematic ground-motion simulations on rough faults including effects of 3D Stochastic velocity PerturbationsKinematic ground-motion simulations on rough faults. Bull. Seismol. Soc. Am. 106 (5), 2136–2153. https://doi.org/10.1785/0120160088.

Gu, C., Meng, X., Wang, S., Ding, X., 2021. Study on the mutual influence of surface roughness and texture features of rough-textured surfaces on the tribological properties. Proc. IME J. J. Eng. Tribol. 235 (2), 256–273. https://doi.org/10.1177/1350650120940211.

Hadizadeh, J., Tullis, T.E., White, J.C., Konkachbaev, A.I., 2015. Shear localization, velocity weakening behavior, and development of cataclastic foliation in experimental granite gouge. J. Struct. Geol. 71, 86–99. https://doi.org/10.1016/j.jsg.2014.10.013.

Han, S., Zhao, L., Jiang, Q., Lian, J., 2012. Deformation-induced localized solid-state amorphization in nanocrystalline nickel. Sci. Rep. 2, 493. https://doi.org/10.1038/srep00493.

Harbord, C.W.A., Nielsen, S.B., De Paola, N., Holdsworth, R.E., 2017. Earthquake nucleation on rough faults. Geology 45 (10), 931–934. https://doi.org/10.1130/G39181.1.

Heesakkers, V., Murphy, S., Reches, Z., 2011. Earthquake rupture at focal depth, Part I: structure and rupture of the pretorius fault, TauTona mine, South Africa. Pure Appl. Geophys. 168 (12), 2395–2425. https://doi.org/10.1007/s00024-011-0354-7.

Heilbronner, R., Barrett, S., 2014. Fractal grain size distributions. In: Heilbronner, R., Barrett, S. (Eds.), Image Analysis in Earth Sciences: Microstructures and Textures of Earth Materials. Springer Berlin Heidelberg, Berlin, Heidelberg, pp. 225–249. https://doi.org/10.1007/978-3-642-10343-8_13.

Hippertt, J., 1999. Are S–C structures, duplexes and conjugate shear zones different manifestations of the same scale-invariant phenomenon? J. Struct. Geol. 21 (8), 975–984. https://doi.org/10.1016/S0191-8141(99)00047-4.

Hoisch, T.D., Miller, C.F., Heizler, M.T., Harrison, T.M., Stoddard, E.F., 1988. Late Cretaceous regional metamorphism in southeastern California. Metamorphism and Crustal Evolution of the Western United States 7, 538–571.

Houser, L.M., Ault, A.K., Newell, D.L., Evans, J.P., Shen, F.-A., Van Devener, B.R., 2021. Nanoscale textural and chemical evolution of silica fault mirrors in the Wasatch fault damage zone, Utah, USA. G-cubed 22 (3). https://doi.org/10.1029/2020gc009368.

Jacobs, T.D.B., Junge, T., Pastewka, L., 2017. Quantitative characterization of surface topography using spectral analysis. Surf. Topography: Metrol. Prop. 5 (1), 013001 https://doi.org/10.1088/2051-672X/aa51f8.

Jordan, P.G., 1987. The deformational behaviour of bimineralic limestone-halite aggregates. Tectonophysics 135 (1), 185–197. https://doi.org/10.1016/0040-1951(87)90160-0.

Kaneki, S., Oohashi, K., Hirono, T., Noda, H., 2020. Mechanical amorphization of synthetic fault gouges during rotary-shear friction experiments at subseismic to seismic slip velocities. J. Geophys. Res. Solid Earth 125 (10). https://doi.org/10.1029/2020jb019956.

Kearse, J., Kaneko, Y., Little, T., Van Dissen, R., 2019. Curved slickenlines preserve direction of rupture propagation. Geology 47 (9), 838–842. https://doi.org/10.1130/G46563.1.

Keulen, N., Heilbronner, R., Stünitz, H., Boullier, A.-M., Ito, H., 2007. Grain size distributions of fault rocks: a comparison between experimentally and naturally deformed granitoids. J. Struct. Geol. 29 (8), 1282–1300. https://doi.org/10.1016/j.jsg.2007.04.003.

Keulen, N., Stünitz, H., Heilbronner, R., 2008. Healing microstructures of experimental and natural fault gouge. J. Geophys. Res. 113 (B6) https://doi.org/10.1029/2007jb005039.

Kim, T.W., Bhushan, B., Cho, Y.J., 2006. The contact behavior of elastic/plastic non-Gaussian rough surfaces. Tribol. Lett. 22 (1), 1. https://doi.org/10.1007/s11249-006-9036-5.

Kirkpatrick, J.D., Brodsky, E.E., 2014. Slickenline orientations as a record of fault rock rheology. Earth Planet Sci. Lett. 408, 24–34. https://doi.org/10.1016/j.epsl.2014.09.040.

Kirkpatrick, J.D., Rowe, C.D., White, J.C., Brodsky, E.E., 2013. Silica gel formation during fault slip: evidence from the rock record. Geology 41 (9), 1015–1018. https://doi.org/10.1130/G34483.1.

Kirkpatrick, J.D., Edwards, J.H., Verdecchia, A., Kluesner, J.W., Harrington, R.M., Silver, E.A., 2020. Subduction megathrust heterogeneity characterized from 3D seismic data. Nat. Geosci. 13 (5), 369–374. https://doi.org/10.1038/s41561-020-0562-9.

Knieke, C., 2012. Fracture at the Nanoscale and the Limit of Grinding: Partikelbruch Im Nanometerbereich und Die Grenze Der Echtzerkleinerung. Cuvillier.

Knieke, C., Romeis, S., Peukert, W., 2011. Influence of process parameters on breakage kinetics and grinding limit at the nanoscale. AIChE J. American Instit. Chem. Eng. 57 (7), 1751–1758. https://doi.org/10.1002/aic.12408.

Kotwal, C.A., Bhushan, B., 1996. Contact analysis of non-Gaussian surfaces for minimum static and kinetic friction and wear. Tribol. Trans. 39 (4), 890–898. https://doi.org/10.1080/10402009608983609.

Kuo, L.-W., Song, S.-R., Suppe, J., Yeh, E.-C., 2016. Fault mirrors in seismically active fault zones: a fossil of small earthquakes at shallow depths. Geophys. Res. Lett. 43 (5), 1950–1959. https://doi.org/10.1002/2015gl066882.

Lee, J.-J., Bruhn, R.L., 1996. Structural anisotropy of normal fault surfaces. J. Struct. Geol. 18 (8), 1043–1059. https://doi.org/10.1016/0191-8141(96)00022-3.

Lee, Y.-J., 1991. In: Means, W. (Ed.), *Slickenside Petrography: Slip-Sense Indicators and Classification* (Master of Sciences). State University of New York at Albany. Retrieved from. http://www.atmos.albany.edu/geology/theses/leeyjmstxt.pdf.

Lin, A., 2001. S–C fabrics developed in cataclastic rocks from the Nojima fault zone, Japan and their implications for tectonic history. J. Struct. Geol. 23 (6), 1167–1178. https://doi.org/10.1016/S0191-8141(00)00171-1.

Lin, S., Williams, P.F., 1992. The origin of ridge-in-groove slickenside striae and associated steps in an S-C mylonite. J. Struct. Geol. 14 (3), 315–321. https://doi.org/10.1016/0191-8141(92)90089-F.

Lin, S., Jiang, D., Williams, P.F., 2007. Importance of differentiating ductile slickenside striations from stretching lineations and variation of shear direction across a high-strain zone. J. Struct. Geol. 29 (5), 850–862. https://doi.org/10.1016/j.jsg.2006.12.006.

Chapter XXXVI. Mineral veins. In: Lyell, S.C. (Ed.), 1871. The Student's Elements of Geology. Thomas Telford Publishing, pp. 589–602. https://doi.org/10.1680/tseog.52581.0036.

Macklin, C., Kaneko, Y., Kearse, J., 2021. Coseismic slickenlines record the emergence of multiple rupture fronts during a surface-breaking earthquake. Tectonophysics 808, 228834. https://doi.org/10.1016/j.tecto.2021.228834.

Mandelbrot, B.B., 1985. Self-affine fractals and fractal dimension. Phys. Scripta 32 (4), 257. https://doi.org/10.1088/0031-8949/32/4/001.

Marti, S., Stünitz, H., Heilbronner, R., Plümper, O., 2020. Amorphous material in experimentally deformed mafic rock and its temperature dependence: implications for fault rheology during aseismic creep and seismic rupture. J. Struct. Geol. 138, 104081 https://doi.org/10.1016/j.jsg.2020.104081.

McCool, J.I., 1992. Non-Gaussian effects in microcontact. Int. J. Mach. Tool Manufact. 32 (1), 115–123. https://doi.org/10.1016/0890-6955(92)90068-R.

McDermott, R.G., Ault, A.K., Evans, J.P., Reiners, P.W., 2017. Thermochronometric and textural evidence for seismicity via asperity flash heating on exhumed hematite fault mirrors, Wasatch fault zone, UT, USA. Earth Planet Sci. Lett. 471, 85–93. https://doi.org/10.1016/j.epsl.2017.04.020.

Milanese, E., Brink, T., Aghababaei, R., Molinari, J.-F., 2019. Emergence of self-affine surfaces during adhesive wear. Nat. Commun. 10 (1), 1116. https://doi.org/10.1038/s41467-019-09127-8.

Miller, C.F., Howard, K.A., Hoisch, T.D., 1982. Mesozoic Thrusting, Metamorphism, and Plutonism, Old Woman-Piute Range, Southeastern California.Mesozoic-Cenozoic Tectonic Evolution of the Colorado River Region, California, Arizona, and Nevada. Cordilleran Publishers, San Diego, California, pp. 561–581.

Nakamura, N., Nagahama, H., 2002. Tribochemical wearing in S-C mylonites and its implication to lithosphere stress level. Earth Planets Space 54 (11), 1103–1108. https://doi.org/10.1186/bf03353309.

Odlum, M.L., Ault, A.K., Channer, M.A., Calzolari, G., 2022. Seismicity recorded in hematite fault mirrors in the Rio Grande rift. Geosphere 18 (1), 241–260. https://doi.org/10.1130/GES02426.1.

Ohl, M., Plümper, O., Chatzaras, V., Wallis, D., Vollmer, C., Drury, M., 2020. Mechanisms of fault mirror formation and fault healing in carbonate rocks. Earth Planet Sci. Lett. 530, 115886 https://doi.org/10.1016/j.epsl.2019.115886.

Ortega-Arroyo, D., 2017. The Rock Record of Seismic Nucleation and Dynamic Weakening: Case Studies from the Whipple Mountains Detachment Fault, Eastern California. University of Texas at Austin.

Otsubo, M., Shigematsu, N., Imanishi, K., Ando, R., Takahashi, M., Azuma, T., 2013. Temporal slip change based on curved slickenlines on fault scarps along Itozawa fault caused by 2011 Iwaki earthquake, northeast Japan. Tectonophysics 608, 970–979. https://doi.org/10.1016/j.tecto.2013.07.022.

Passchier, C.W., Trouw, R.A.J., 2005. Microtectonics. Springer, Berlin, Heidelberg. https://doi.org/10.1007/3-540-29359-0.

Pec, M., Al Nasser, S., 2021. Formation of nanocrystalline and amorphous materials causes parallel brittle-viscous flow of crustal rocks: experiments on quartz-feldspar aggregates. J. Geophys. Res. Solid Earth 126 (5). https://doi.org/10.1029/2020jb021262.

Pec, M., Stünitz, H., Heilbronner, R., Drury, M., de Capitani, C., 2012a. Origin of pseudotachylites in slow creep experiments. Earth Planet Sci. Lett. 355–356, 299–310. https://doi.org/10.1016/j.epsl.2012.09.004.

Pec, M., Stünitz, H., Heilbronner, R., 2012b. Semi-brittle deformation of granitoid gouges in shear experiments at elevated pressures and temperatures. J. Struct. Geol. 38, 200–221.

Pec, M., Stünitz, H., Heilbronner, R., Drury, M., 2016. Semi-brittle flow of granitoid fault rocks in experiments. J. Geophys. Res. Solid Earth 121 (3), 1677–1705. https://doi.org/10.1002/2015jb012513.

Petit, J.P., 1987. Criteria for the sense of movement on fault surfaces in brittle rocks. J. Struct. Geol. 9 (5), 597–608. https://doi.org/10.1016/0191-8141(87)90145-3.

Power, W.L., Tullis, T.E., 1989. The relationship between slickenside surfaces in fine-grained quartz and the seismic cycle. J. Struct. Geol. 11 (7), 879–893. https://doi.org/10.1016/0191-8141(89)90105-3.

Power, W.L., Tullis, T.E., Brown, S.R., Boitnott, G.N., Scholz, C.H., 1987. Roughness of natural fault surfaces. Geophys. Res. Lett. 14 (1), 29–32. https://doi.org/10.1029/gl014i001p00029.

Renard, F., Mair, K., Gundersen, O., 2012. Surface roughness evolution on experimentally simulated faults. J. Struct. Geol. 45, 101–112. https://doi.org/10.1016/j.jsg.2012.03.009.

Reynolds, S.J., Richard, S.M., Haxel, G.B., Tosdal, R.M., Laubach, S.E., Ernst, W.G., 1988. Geologic Setting of Mesozoic and Cenozoic Metamorphism in Arizona. Metamorphism and Crustal Evolution of the Western United States (Rubey Volume 7). Prentice Hall, Englewood Cliffs, New Jersey, pp. 466–501.

Rice, J.R., 2006. Heating and weakening of faults during earthquake slip. J. Geophys. Res. 111 (B5) https://doi.org/10.1029/2005jb004006.

Ring, T.E., Fletcher, J.M., Kelly, M.M., Karlstrom, K.E., 1988. Mesozoic crustal shortening by deep-seated tectonic wedging along Proterozoic anisotropies, Piute Mountains, southeastern California: geol. Soc. America (Abs. with Prog.) 20, 224.

Romeis, S., Schmidt, J., Peukert, W., 2016. Mechanochemical aspects in wet stirred media milling. Int. J. Miner. Process. 156, 24–31. https://doi.org/10.1016/j.minpro.2016.05.018.

Rosas-Elguera, J., Ferrari, L., Garduño-Monroy, V.H., Urrutia-Fucugauchi, J., 1996. Continental boundaries of the Jalisco block and their influence in the Pliocene-Quaternary kinematics of western Mexico. Geology 24 (10), 921–924. https://doi.org/10.1130/0091-7613(1996)024<0921:CBOTJB>2.3.CO;2.

Rowe, C.D., Ross, C., Swanson, M.T., Pollock, S., Backeberg, N.R., Barshi, N.A., et al., 2018. Geometric complexity of earthquake rupture surfaces preserved in pseudotachylyte networks. J. Geophys. Res. Solid Earth 123 (9), 7998–8015. https://doi.org/10.1029/2018jb016192.

Rowe, C.D., Lamothe, K., Rempe, M., Andrews, M., Mitchell, T.M., Di Toro, G., et al., 2019. Earthquake lubrication and healing explained by amorphous nanosilica. Nat. Commun. 10 (1), 320. https://doi.org/10.1038/s41467-018-08238-y.

Sagy, A., Lyakhovsky, V., 2019. Stress patterns and failure around rough interlocked fault surface. J. Geophys. Res. Solid Earth 124 (7), 7138–7154. https://doi.org/10.1029/2018jb017006.

Sagy, A., Brodsky, E.E., Axen, G.J., 2007. Evolution of fault-surface roughness with slip. Geology 35 (3), 283–286. https://doi.org/10.1130/G23235A.1.

Scholz, C.H., 2019. The Mechanics of Earthquakes and Faulting (3rd ed.). Cambridge University Press, Cambridge. https://doi.org/10.1017/9781316681473.

Sedlaček, M., Podgornik, B., Vižintin, J., 2012. Correlation between standard roughness parameters skewness and kurtosis and tribological behaviour of contact surfaces. Tribol. Int. 48, 102–112. https://doi.org/10.1016/j.triboint.2011.11.008.

Shervais, K.A.H., Kirkpatrick, J.D., 2016. Smoothing and re-roughening processes: the geometric evolution of a single fault zone. J. Struct. Geol. 91, 130–143. https://doi.org/10.1016/j.jsg.2016.09.004.

Siman-Tov, S., Aharonov, E., Sagy, A., Emmanuel, S., 2013. Nanograins form carbonate fault mirrors. Geology 41 (6), 703–706. https://doi.org/10.1130/G34087.1.

Siman-Tov, S., Aharonov, E., Boneh, Y., Reches, Z., 2015. Fault mirrors along carbonate faults: formation and destruction during shear experiments. Earth Planet Sci. Lett. 430, 367–376. https://doi.org/10.1016/j.epsl.2015.08.031.

Sun, H., Pec, M., 2021. Nanometric flow and earthquake instability. Nat. Commun. 12 (1), 6779. https://doi.org/10.1038/s41467-021-26996-0.

Swanson, M.T., 1988. Pseudotachylyte-bearing strike-slip duplex structures in the fort foster brittle zone, S. Maine. J. Struct. Geol. 10 (8), 813–828. https://doi.org/10.1016/0191-8141(88)90097-1.

Tal, Y., Goebel, T., Avouac, J.-P., 2020. Experimental and modeling study of the effect of fault roughness on dynamic frictional sliding. Earth Planet Sci. Lett. 536 (116133), 116133 https://doi.org/10.1016/j.epsl.2020.116133.

Tayebi, N., Polycarpou, A.A., 2004. Modeling the effect of skewness and kurtosis on the static friction coefficient of rough surfaces. Tribol. Int. 37 (6), 491–505. https://doi.org/10.1016/j.triboint.2003.11.010.

Taylor, M.P., Ault, A.K., Odlum, M.L., Newell, D.L., 2021. Shallow rupture propagation of Pleistocene earthquakes along the hurricane fault, UT, revealed by hematite (U-Th)/he thermochronometry and textures. Geophys. Res. Lett. 48 (17) https://doi.org/10.1029/2021gl094379.

Thom, C.A., Brodsky, E.E., Carpick, R.W., Pharr, G.M., Oliver, W.C., Goldsby, D.L., 2017. Nanoscale roughness of natural fault surfaces controlled by scale-dependent yield strength. Geophys. Res. Lett. 44 (18), 9299–9307. https://doi.org/10.1002/2017gl074663.

Tikoff, B., Chatzaras, V., Newman, J., Roberts, N.M., 2019. Big data in microstructure analysis: building a universal orientation system for thin sections. J. Struct. Geol. 125, 226–234. https://doi.org/10.1016/j.jsg.2018.09.019.

Tisato, N., Di Toro, G., De Rossi, N., Quaresimin, M., Candela, T., 2012. Experimental investigation of flash weakening in limestone. J. Struct. Geol. 38, 183–199. https://doi.org/10.1016/j.jsg.2011.11.017.

Tomota, T., Kondoh, Y., Ohmori, T., 2019. Modeling solid contact between smooth and rough surfaces with non-Gaussian distributions. Tribol. Trans. 62 (4), 580–591. https://doi.org/10.1080/10402004.2019.1573341.

Torabi, A., Ellingsen, T.S.S., Johannessen, M.U., Alaei, B., Rotevatn, A., Chiarella, D., 2020. Fault zone architecture and its scaling laws: where does the damage zone start and stop? Geological Society, London, Special Publications 496 (1), 99–124. https://doi.org/10.1144/SP496-2018-151.

Torabi, A., Balsamo, F., Nogueira, F.C.C., Vasconcelos, D.L., Silva, A.C.E., Bezerra, F.H. R., Souza, J.A.B., 2021. Variation of thickness, internal structure and petrophysical properties in a deformation band fault zone in siliciclastic rocks. Mar. Petrol. Geol. 133, 105297 https://doi.org/10.1016/j.marpetgeo.2021.105297.

Toy, V.G., Niemeijer, A., Renard, F., Morales, L., Wirth, R., 2017. Striation and slickenline development on quartz fault surfaces at crustal conditions: origin and effect on friction. J. Geophys. Res. Solid Earth 122 (5), 3497–3512. https://doi.org/10.1002/2016jb013498.

Tsai, V.C., Hirth, G., 2020. Elastic impact consequences for high-frequency earthquake ground motion. Geophys. Res. Lett. 47 (5) https://doi.org/10.1029/2019gl086302.

Tsai, V.C., Hirth, G., Trugman, D.T., Chu, S.X., 2021. Impact versus frictional earthquake models for high-frequency radiation in complex fault zones. J. Geophys. Res. Solid Earth 126 (8). https://doi.org/10.1029/2021jb022313.

Ulrich, T., Gabriel, A.-A., Ampuero, J.-P., Xu, W., 2019. Dynamic viability of the 2016 Mw 7.8 Kaikōura earthquake cascade on weak crustal faults. Nat. Commun. 10 (1), 1213. https://doi.org/10.1038/s41467-019-09125-w.

Verberne, B.A., Plümper, O., de Winter, D.A.M., Spiers, C.J., 2014. Rock mechanics. Superplastic nanofibrous slip zones control seismogenic fault friction. Science 346 (6215), 1342–1344. https://doi.org/10.1126/science.1259003.

Verberne, B.A., Plümper, O., Spiers, C.J., 2019. Nanocrystalline principal slip zones and their role in controlling crustal fault rheology. Minerals 9 (6), 328. https://doi.org/10.3390/min9060328.

Viat, A., Guillonneau, G., Fouvry, S., Kermouche, G., Sao Joao, S., Wehrs, J., et al., 2017. Brittle to ductile transition of tribomaterial in relation to wear response at high temperatures. Wear: Int. J. Sci. Technol. Friction Lubricat. Wear 60–68. https://doi.org/10.1016/j.wear.2017.09.015, 392–393.

Viti, C., Brogi, A., Liotta, D., Mugnaioli, E., Spiess, R., Dini, A., et al., 2016. Seismic slip recorded in tourmaline fault mirrors from Elba Island (Italy). J. Struct. Geol. 86, 1–12. https://doi.org/10.1016/j.jsg.2016.02.013.

Wang, M., Chen, Y.-F., Ma, G.-W., Zhou, J.-Q., Zhou, C.-B., 2016. Influence of surface roughness on nonlinear flow behaviors in 3D self-affine rough fractures: lattice Boltzmann simulations. Adv. Water Resour. 96, 373–388. https://doi.org/10.1016/j.advwatres.2016.08.006.

Wang, W.-Z., Chen, H., Hu, Y.-Z., Wang, H., 2006. Effect of surface roughness parameters on mixed lubrication characteristics. Tribol. Int. 39 (6), 522–527. https://doi.org/10.1016/j.triboint.2005.03.018.

Will, T.M., Wilson, C.J.L., 1989. Experimentally produced slickenside lineations in pyrophyllitic clay. J. Struct. Geol. 11 (6), 657–667. https://doi.org/10.1016/0191-8141(89)90002-3.

Wilson, C.J.L., Will, T.M., 1990. Slickenside lineations due to ductile processes. Geological Society, London, Special Publications 54 (1), 455–460. https://doi.org/10.1144/GSL.SP.1990.054.01.41.

Yan, X.-L., Wang, X.-L., Zhang, Y.-Y., 2014. Influence of roughness parameters skewness and kurtosis on fatigue life under mixed elastohydrodynamic lubrication point contacts. J. Tribol. 136 (3) https://doi.org/10.1115/1.4027480.

Zhang, S., Wang, W., Zhao, Z., 2014. The effect of surface roughness characteristics on the elastic–plastic contact performance. Tribol. Int. 79, 59–73. https://doi.org/10.1016/j.triboint.2014.05.016.

Zhang, Y.S., Zhang, L.C., Niu, H.Z., Bai, X.F., Yu, S., Ma, X.Q., Yu, Z.T., 2014. Deformation twinning and localized amorphization in nanocrystalline tantalum induced by sliding friction. Mater. Lett. 127, 4–7. https://doi.org/10.1016/j.matlet.2014.04.079.

Zhao, S., Hahn, E.N., Kad, B., Remington, B.A., Wehrenberg, C.E., Bringa, E.M., Meyers, M.A., 2016. Amorphization and nanocrystallization of silicon under shock compression. Acta Mater. 103, 519–533. https://doi.org/10.1016/j.actamat.2015.09.022.